

# Design of the Cosmology Large Angular Scale Surveyor (CLASS) Polarization Modulators

Nicholas Mehrle

Advisor: Dr Tobias Marriage

*Johns Hopkins University*

July 31, 2016

## Abstract

A popular, yet unproven theory about the origins of the universe concerns the epoch of inflation, wherein the universe grew exponentially within the first  $\sim 10^{-34}$  s after the Big Bang. In this thesis, we discuss one of the leading experiments aimed at detecting evidence for inflation, the Cosmology Large Angular Scale Surveyor (CLASS). We present a cosmological background aimed at a typical undergraduate student with little to no experience in the field. We then discuss the CLASS experiment with emphasis on the CLASS variable-delay polarization modulators (VPMs). The VPMs are a crucial element of the experiment and allow CLASS to make the necessary polarization measurements vital to a detection of inflation. A VPM consists of a wire-grid polarization separator and a movable mirror that together introduce a phase delay between orthogonal polarization states. We explain the operation of and model a CLASS VPM. We discuss the mirror transport mechanism (MTM) in detail including its design and control. We estimate and measure the spring constants of the MTM system.

## Acknowledgements

I would like to first thank Professor Tobias Marriage. Toby welcomed me onto the CLASS experiment the summer after my freshman year and has provided mentoring and support ever since. My experience on the telescope has proven invaluable in helping me learn and develop as a scientist and as a person. I would also like to thank Joseph Eimer and Katie Harrington for answering so many questions and guiding me through this project, and of course Professor Charles Bennett without whom the CLASS telescope would not exist. The entire CLASS collaboration at JHU has been incredibly warm and welcoming to me and I would like to thank each and every person involved.

Finally I owe enormous gratitude to my fellow graduates from the CLASS experiment, Manwei Chan and Zhuo (Ben) Zhang for their support through late nights and early mornings.

# Contents

<b>1</b>	<b>Cosmology Background</b>	<b>1</b>
1.1	Foundations . . . . .	1
1.2	History . . . . .	3
1.3	Cosmic Microwave Background . . . . .	5
1.3.1	Origin . . . . .	5
1.3.2	Temperature Anisotropies . . . . .	7
1.3.3	Polarization . . . . .	8
1.3.4	E and B modes . . . . .	11
1.4	Inflation . . . . .	13
1.4.1	Problems in $\Lambda$ CDM . . . . .	13
1.4.2	Inflation Solution . . . . .	15
1.4.3	Inflationary observables . . . . .	17
<b>2</b>	<b>Cosmology Large Angular Scale Surveyor (CLASS)</b>	<b>18</b>
2.1	Experimental Details . . . . .	20
2.2	Foregrounds . . . . .	21
2.2.1	Lensing . . . . .	23
2.3	Optical Design . . . . .	23
2.3.1	Cryostat . . . . .	25
2.3.2	Detectors . . . . .	26
<b>3</b>	<b>Variable-Delay Polarization Modulator</b>	<b>27</b>

3.1	Operation . . . . .	27
3.1.1	Mathematical Interpretation . . . . .	29
3.2	Benefits . . . . .	32
3.2.1	$1/f$ noise . . . . .	32
3.3	Design . . . . .	34
3.3.1	Wire Grid . . . . .	35
<b>4</b>	<b>Mirror Transport Mechanism</b>	<b>36</b>
4.1	Flexures . . . . .	37
4.1.1	Predicted Compliance . . . . .	38
4.1.2	Measurement of Compliance . . . . .	41
4.2	Electronic Components . . . . .	44
4.2.1	Voice Coils . . . . .	44
4.2.2	Linear Encoders . . . . .	44
4.2.3	Vibration Sensor . . . . .	45
4.3	Control Systems . . . . .	45
4.3.1	Model . . . . .	45
4.3.2	CLASS control systems . . . . .	48
<b>5</b>	<b>Summary</b>	<b>50</b>
<b>Appendices</b>		<b>51</b>
<b>A</b>	<b>Optical Background</b>	<b>52</b>
A.1	Polarized light . . . . .	52
A.2	Stokes Parameters . . . . .	55
A.2.1	Rotations . . . . .	57
A.2.2	Stokes Vectors . . . . .	57
A.3	Jones Matrices . . . . .	58

<b>B Thomson Scattering</b>	<b>60</b>
B.1 Unpolarized Incident Light . . . . .	62
<b>C Curvature of the Universe</b>	<b>64</b>
<b>References</b>	<b>66</b>

# Chapter 1

## Cosmology Background

Cosmology is the study of the cosmos. As a field, it seeks to answers questions like “What is out there beyond our Solar System?”, “How long ago did the universe form?”, and “What has happened since then?”. The current standard model for cosmology is known as the  $\Lambda$ CDM model, which describes a universe filled not only with the matter and energy we are familiar with, but also with dark energy ( $\Lambda$ ) and non-relativistic matter that doesn’t interact with light, called cold dark matter (CDM). In this chapter, we will explore the foundations of modern cosmology and give a brief history of the universe. We will describe one potential extension to the  $\Lambda$ CDM model, known as inflation, which is of particular interest for this paper as the CLASS telescope hopes to find evidence for it.

### 1.1 Foundations

Modern cosmology is based on the cosmological principle, and Einstein’s theory of general relativity. The cosmological principle states that on large scales, space is both homogeneous (the same in all places), and isotropic (the same in all directions). Thus, there is no preferred place or direction in the universe. Einstein’s theory of relativity is itself based on three ideas: the equivalence principle, Fermat’s principle and his theory of special relativity. The equivalence principle (1.1.3) states that an objects inertial mass (as appearing in Newton’s 2nd law (1.1.1)) and it’s gravitational mass (as

appearing in Newton's law of gravity (1.1.2)) are equal.

$$F = m_i a \quad (1.1.1)$$

$$F_g = -G \frac{M_g m_g}{r^2} \quad (1.1.2)$$

$$m_i = m_g \quad (1.1.3)$$

Equivalence Principle

Fermat's principle states that the path light takes to travel between two points is that which minimizes travel time. In a vacuum this translates to light taking the shortest path between two objects. Einstein combined these ideas with special relativity to conclude that the presence of mass-energy causes space-time to bend, creating a non-euclidean geometry for spacetime. This conclusion can be most easily understood through a classic thought experiment Einstein created. Suppose you are standing on the surface of the Earth, and you drop a ball. You observe the ball falling to the ground at an acceleration of  $9.8 \text{ m s}^{-2}$ . Now suppose you are in a spaceship in a vacuum accelerating upwards at  $9.8 \text{ m s}^{-2}$ , and you drop a ball. You will see the ball fall to the floor of the ship with the same acceleration. Now, suppose instead of knowing where you were, you find yourself inside a sealed box. You drop a ball and observe it fall with an acceleration of  $9.8 \text{ m s}^{-2}$ . From this observation you cannot conclude if you are on the surface of the earth, or in a spaceship. This is the equivalence principle.

Now, instead of dropping a ball, suppose you shine a flashlight horizontally onto a wall. If you are in the spaceship, during the time it takes the light to travel from your flashlight to the wall the spaceship will move upwards due to its acceleration, causing the light to strike the wall below the flashlight. The light curves downward due to the acceleration of the ship. Einstein used the equivalence principle to conclude that the same will happen on the surface of the earth - that the light would curve downwards due to the Earth's gravity. Since, by Fermat's principle we know that light takes the shortest path between two points, we must conclude that this curved path is the shortest path. Thus, space-time must be curved due to the gravity of the Earth.

## 1.2 History

The universe began as a singularity when all matter and energy existed in an infinitely dense point. Starting approximately 13.8 billion years ago, space began to expand in an event known as the Big Bang. There is substantial evidence for the Big Bang that is beyond the scope of this document. We will mention, however, that throughout its history and even now, space is expanding homogeneously and isotropically. The initial evidence for this was observed by Edwin Hubble in 1929, when he discovered that galactic redshift was proportional to the distance of the galaxy from Earth[32]. This cosmic redshift ( $z$ ) is analogous to a Doppler effect in that it is the normalized difference between the wavelength of emitted light  $\lambda_{em}$  and the observed wavelength  $\lambda_{ob}$  resulting from source moving relative to the observer. It is defined by equation 1.2.1.

$$z \equiv \frac{\lambda_{ob} - \lambda_{em}}{\lambda_{em}} \quad (1.2.1)$$

Hubble observed that redshift increases with distance. This allows us to do two things. First, since redshift is related to how far away something is, and the light allowing us to observe that something travels at a finite speed, we can use redshift to measure time on cosmic scales, and  $z \gg 1$  corresponds to times in the distant past. Second, we can conclude that nearby galaxies are moving away from us, and farther away galaxies are moving away faster. Because of the cosmological principle, we conclude not that space is expanding around the Earth, but that all space is undergoing a homogenous, isotropic expansion. If this expansion is extrapolated backwards in time, it is consistent with space originating from a singularity roughly 14 billion years ago, giving the initial evidence for the Big Bang.

The universe is composed of three components. There is matter (comprising of both baryonic and dark matter) radiation (consisting of photons and neutrinos), and dark energy. Each component has, at one point, been the dominant component of the energy density of the universe, and each causes the universe to expand at different rates when dominant. This expansion is described in terms of a scale factor,  $a(t)$  which is the size of the universe relative to its current size. Originally the universe was dominated by radiation and the scale factor went as  $a \propto t^{1/2}$ . Around approximately

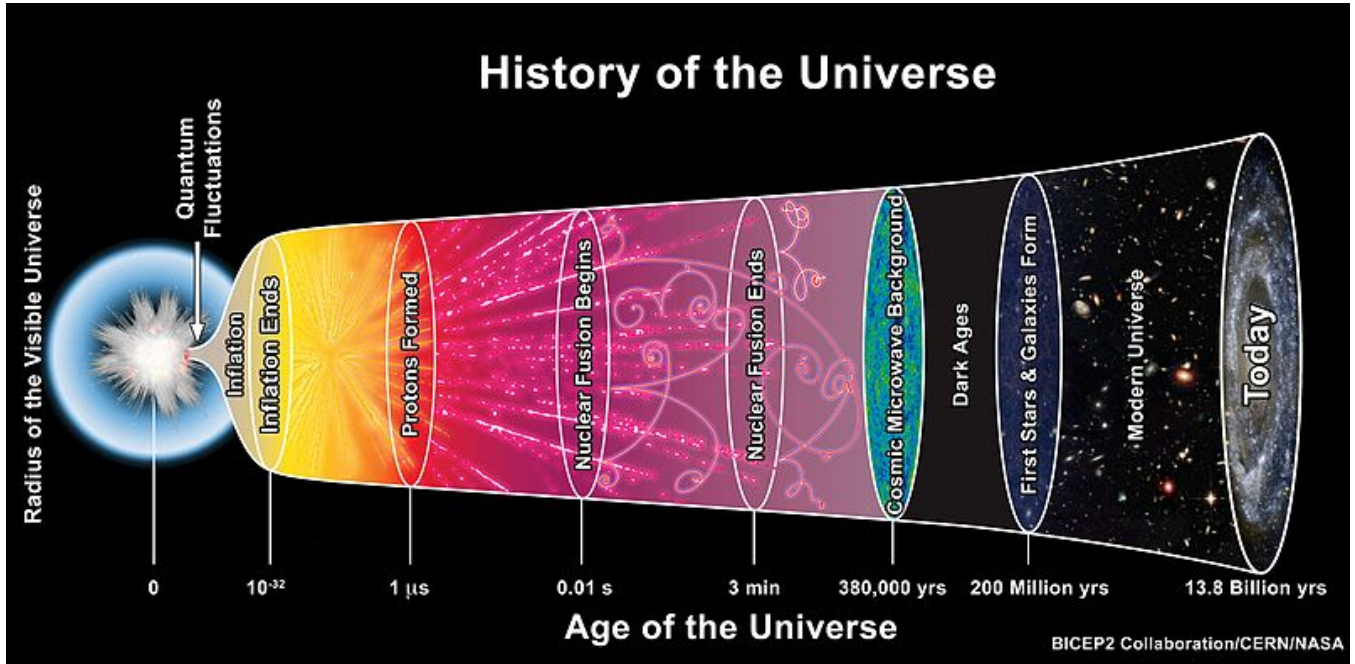


Figure 1.1: A plot of the history of the Universe showing important epochs. As the universe evolved its size has grown and it has now entered a period of accelerated expansion. [34]

47,000 years after the Big Bang, the contribution from matter became the dominant contribution to the energy density of the universe. Here, the universe entered the era of matter domination in which the scale factor went as  $a \propto t^{2/3}$ . Roughly 9.8 billion years after the Big Bang, dark energy became dominant and the expansion began to accelerate rapidly with  $a \propto e^{Kt}$  [32].

As the universe expands, it cools which causes its structure to change over time. Very early on, the mean temperature in the universe was very high, and space was filled with a hot plasma made up of quarks and gluons. As the universe cooled quarks came together to form protons and neutrons [4]. At  $t \sim 2$  sec (i.e. 2 seconds after the Big Bang), these joined to form the lighter nuclei (of which the stable ones are H, D,  $^3\text{He}$ ,  $^4\text{He}$ ,  $^6\text{Li}$ , and  $^7\text{Li}$ ), in a process called Big Bang Nucleosynthesis. Of the nuclei produced, the majority are H (i.e. a free proton) with some  $^4\text{He}$ , with the rest in trace amounts. At  $t \sim 10$  min the universe had cooled enough that Nucleosynthesis ends [32]. At this point, the universe is still ionized. It has not cooled enough for electrons and positively charged nuclei to bind together. This doesn't occur until  $t \sim 240,000$  yr ( $z \approx 1300$ ) when the number density of ions and neutral atoms is equivalent, at what is known as the epoch of recombination. Shortly after this, photons will decouple from matter and then travel freely from the

surface of last scattering creating the Cosmic Microwave Background (CMB), as will be discussed later. After decoupling, the universe becomes transparent to light and the only radiation produced was the 21cm line from neutral hydrogen. Because (almost) no radiation was produced, this period is known as the Dark Ages. The universe remains dark and unionized until much later. Once stars begin to form their light re-ionizes neutral atoms in the universe in the epoch of reionization. There is evidence that this process began roughly 200 million years after the big bang at  $z \sim 20$  and went on until roughly a billion years after at  $z \sim 6$  [4].

## 1.3 Cosmic Microwave Background

The universe is filled with a (mostly) isotropic blackbody radiation which can be observed at all points in space. This radiation has mean temperature  $T = 2.725\text{K}$  corresponding to photons with wavelengths in the microwave region. Because this radiation is a constant presence, and is in the microwave region, we call it the Cosmic Microwave Background (CMB). Originally detected accidentally by Arno Penzias and Robert Wilson in 1964, it has since been identified as radiation remnant from the Big Bang [32]. Since then it has been accurately and repeatedly measured, notably first by NASA's Cosmic Background Explorer (COBE). It has also been observed to be polarized, first by the Degree Angular Scale Interferometer (DASI).

CMB photons were emitted from a time relatively close to the Big Bang, and as such they serve as a probe to the state of the universe in its early history. Observing them gives insight into the origin and evolution of the universe. Measurements of the CMB have led to great advances in cosmology and future measurements hold great promise for unveiling more secrets of the universe.

### 1.3.1 Origin

CMB photons originate from the boundary between a time when the universe was opaque to photons and the time it became transparent to them, as it is now. This is known as the epoch of last scattering, and is shortly after the epoch of recombination described before. In between the two is an important epoch known as photon decoupling [32].

The dominant scattering process for cosmic photons in this period is Thomson scattering, as

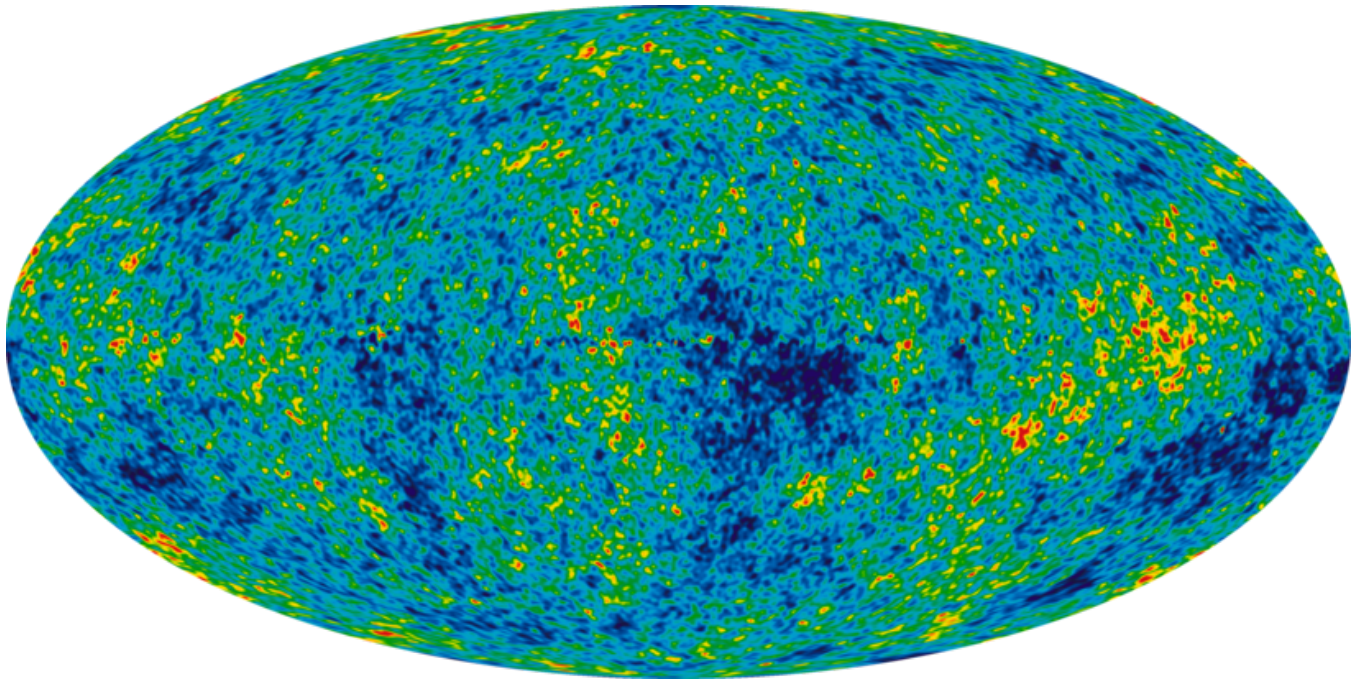


Figure 1.2: The full sky 9-year WMAP CMB Temperature anisotropy map, with galactic foreground removed. The colors represent temperature deviations from the average, with dark blue being  $-200 \mu\text{K}$  and dark red being  $+200 \mu\text{K}$  [30]

discussed in Appendix B. This is the process by which a photon scatters non-relativistically off of a free electron. Before recombination, the majority of electrons in the universe were free, and photons could not travel far without a scattering event. When the average photon in the universe experienced many scattering events, we say that the universe was optically thick, or opaque to light. At recombination, the number density of free electrons reaches the number of density of bound electrons and Thomson scattering becomes more rare. As free electrons become bound to nuclei, the rate of Thomson scattering decreases. Simultaneously the universe is expanding and the free electron density falls further. We call the point where the rate of expansion of the universe equals the rate of cosmic photon scattering the epoch of photon decoupling. Once this point is reached the likelihood of a photon scattering falls dramatically. Shortly after, the average cosmic photon undergoes its last scattering event at the epoch of last scattering [32]. This occurs at  $t \approx 380,000 \text{ yr}$  or  $z \approx 1100$ . Here, the universe becomes transparent to photons. These photons then travel freely through space (and are redshifted) until they are detected from Earth as the CMB. As this happens at all points on the sky, we observe these photons originating spherical shell

of radius  $4 \times 10^{28}$  cm from which the CMB photons we observe have originated. This is called the surface of last scattering [4]. In reality CMB photons do not undergo last scattering at the same time and the last scattering surface has some depth to it. The surface we refer to corresponds to the average time when CMB photons scattered last.

### 1.3.2 Temperature Anisotropies

The CMB has been measured to have temperature anisotropies on order of  $\Delta T/T = 10^{-5}$  [17]. These variations result from density variations of the same order in the hot early universe [4]. As the universe evolved, these tiny fluctuations were amplified by gravity. Regions that were slightly over-dense had a gravitational pull that attracted surrounding matter causing the region to grow. This gravitational instability led these fluctuations to grow into the galaxies and clusters we see today, and is responsible for the large scale structure of the universe.

CMB temperature anisotropies are described by their correlation function  $C_l$ . This is obtained by first expanding the temperature fluctuations in terms of spherical harmonics

$$\frac{\Delta T}{T}(\theta, \phi) = \sum_{l=0}^{\infty} \sum_{m=-l}^l a_{lm} Y_{lm}(\theta, \phi) \quad (1.3.1)$$

And then averaging the product of the coefficients  $a_{lm}$  over a given multipole moment ( $l$ )

$$\langle a_{l'm'}^* a_{lm} \rangle_l = \delta_{ll'} \delta_{mm'} C_l \quad (1.3.2)$$

This quantity falls rapidly with  $l$  so it is customary to plot the quantity

$$\frac{l(l+1)}{2\pi} C_l \langle T \rangle^2$$

which gives the contribution per logarithmic interval in  $l$  to the temperature fluctuation of the CMB, called the temperature power spectrum [32]. Figure 1.3 shows the power spectrum for CMB temperature anisotropies as measured by a collection of experiments. It is plotted for both the

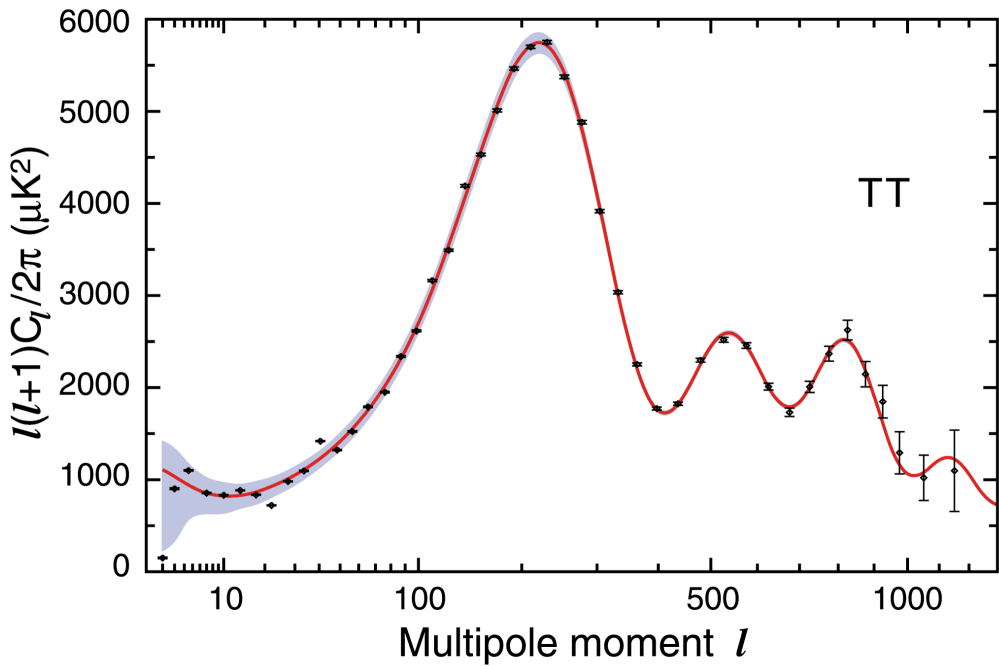


Figure 1.3: The 9 year WMAP CMB TT angular power spectrum. The black points are the WMAP data with error bars, and the best fit model is in red. The blue shaded region represents fundamental limits on how well the TT spectrum can be measured at low multipole. Courtesy of the WMAP science team. [15]

multipole moment  $l$  and angular scale  $\theta$ . The two are related as

$$\theta \propto \frac{\pi}{l}$$

Large angular scales correspond to small  $l$  and small angular scales correspond to large  $l$ .

The series of peaks and troughs shown in the power spectrum were predicted by theory and contain information about the content and shape of the universe. They originate from oscillations in the baryonic fluid before recombination. Measurements of these oscillations have indicated that the universe is nearly spatially flat and have shown that baryonic matter accounts for only  $\sim 4\%$  of the energy density of the universe [16].

### 1.3.3 Polarization

In addition to temperature anisotropies, the CMB contains a polarization pattern, with polarized signal at the  $10^{-6}$  level. The process by which CMB photons are polarized is Thomson scattering

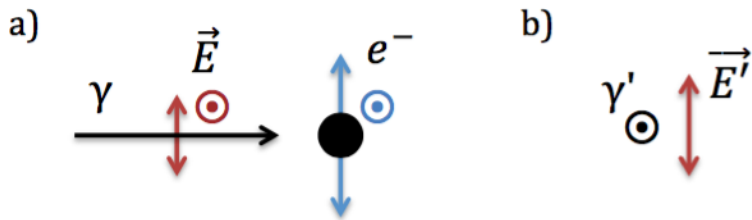


Figure 1.4: Thomson Scattering of unpolarized polarized light off free electron. a) Light ( $\gamma$ ) with polarization components ( $\vec{E}$ ) into and vertical on the page given by the red arrows is incident on a free electron causing it to oscillate with components given by the blue arrows. b) An observer looking down on the page will see scattered light  $\gamma'$  with polarization ( $\vec{E}'$ ) given by the second red arrow. The scattered light is linearly polarized and parallel to one component of the incident light's polarization.

from quadrupole anisotropies. This process creates a linear polarization, with no circularly polarized component.

CMB photons were polarized from Thomson scattering at the surface of last scattering, or after reionization began [4]. Before last scattering, photons scattered rapidly and were randomly polarized producing no net polarization. Between last scattering and reionization there were no free electrons for photons to scatter from, and so only those epochs mentioned contribute to CMB polarization. Because the free electron density was much smaller for reionization, it only contributes about 10 – 20% to the overall polarization pattern. Thomson scattering and the process through which it creates polarization is treated in more depth in Appendix B, but we will present a qualitative argument here.

When light is incident on a free electron with  $h\nu \ll m_e c^2$ , it undergoes Thomson scattering. This condition holds both at the surface of last scattering, and later during reionization. The incident light causes the electron to oscillate in the direction of its electric field. The oscillating electron then emits radiation peaking with intensity perpendicular to, and (linear) polarization parallel to its oscillations (i.e. the direction of the incoming light's polarization). If unpolarized radiation comes in to an electron along the line of sight, the scattered light has equal polarization components in all directions normal to its travel, and remains unpolarized. Suppose now that unpolarized light is

incident on an electron from a direction normal to the observer's line of sight. The light will have components polarized both normal to and along the line of sight. The component normal to the line of sight will Thomson scatter as normal and the observer will see linearly polarized light. The other component causes the electron to oscillate along the line of sight, which does not emit radiation seen by the observer. The end result is that an incident unpolarized beam of light Thomson scatters to produce radiation which peaks linearly polarized in a direction normal to the incident light-line of sight plane.

We now consider not just a single beam of incoming radiation, but a radiation field from all directions, which is unpolarized. If this field is isotropic, the scattered light has polarization components equal in all directions, and so remains unpolarized. If the incoming radiation field has a dipole anisotropy, polarization contributions from the hot and cold incoming radiation will be aligned. In terms of Thomson scattering, this means the electron does not oscillate preferentially in any one direction and the scattered light remains unpolarized. If then there is a quadrupolar temperature anisotropy, the polarization contributions from hot and cold incoming radiation will be aligned  $90^\circ$  to one another. This causes the electron to oscillate preferentially along the axis connecting the cold regions. In turn, the scattered radiation will be linearly polarized in that same direction.

Thus, Thomson scattering can only produce polarization if there is a quadrupolar anisotropy in the incident radiation field. If we decompose the incident radiation field in terms of spherical harmonics  $Y_{lm}(\theta, \phi)$ , only the components with multipole  $l = 2$  generate polarization [17].

As the scattering of CMB photons can be described by  $l = 2$  spherical harmonics, we see there are five modes which contribute:  $m = 0, \pm 1, \pm 2$ . The orthogonality of spherical harmonics dictates that only these modes can contribute. They describe three distinct sources: scalar, vector and tensor perturbations. Scalar modes are density perturbations in the cosmic fluid, vector modes represent vortical motions (divergence-less, curling motions) of the fluid, and tensor perturbations are gravitational waves. Vector modes are damped by the expansion of the universe, and do not contribute to the observed polarization of the CMB. We need only concern ourselves with scalar and tensor perturbations. More information on these modes can be found in Hu and White's *A CMB Polarization Primer*[17].

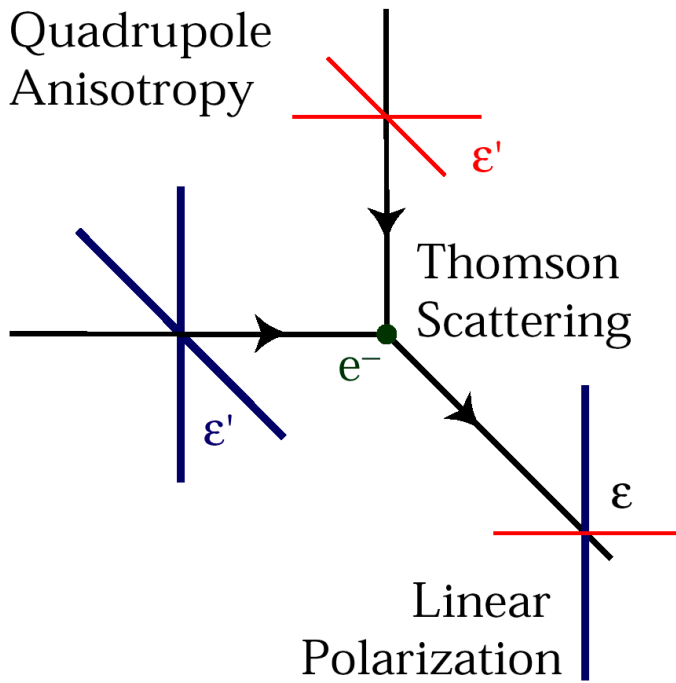


Figure 1.5: Thomson Scattering from a quadrupolar anisotropy in an unpolarized radiation field. Unpolarized light with polarization components  $\epsilon'$  is incident on a free electron. Blue lines represent hot and red lines represent cold radiation. The scattered light is linearly polarized ( $\epsilon$ ) in a direction pointing to the original cold spots. Figure by Wayne Hu [17].

### 1.3.4 E and B modes

In this section we discuss how CMB polarization is typically described. Standard polarization is often described in terms of the Stokes parameters,  $(I, Q, U, V)$ , with linear polarization described by  $(Q, U)$  (See section A.2). It is not possible, however, to define a rotationally invariant basis for  $Q$  and  $U$  on a sphere, like the CMB's surface of last scattering. As such to describe polarization on a sphere, it is traditional to use the basis of  $E$  (electric) and  $B$  (magnetic) modes.

$E$  and  $B$  modes are complex linear combinations of  $Q$  and  $U$  that are rotationally invariant. Whereas  $Q$  and  $U$  are properties about a specific point,  $E$  and  $B$  modes are defined around each point. Thus, they are not local quantities. They are analogous to the decomposition of a vector field into gradient and curl components.  $E$  modes are the analog of the gradient component, and  $B$  modes the curl component. While they are invariant under rotations, each behaves differently under a parity transformation about their center point.  $E$  modes are even under parity, and  $B$  modes are odd. They can be seen along with a decomposition of a temperature (polarization) map into  $E$  and  $B$  modes in figure 1.6.

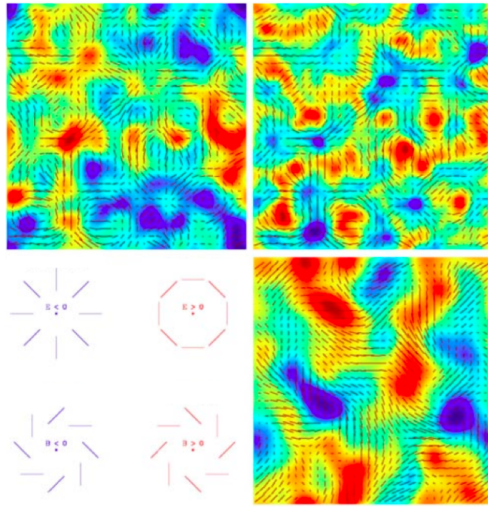


Figure 1.6: **Top Left:** A simulated CMB temperature map with polarization rods. **Top Right:** A map of the corresponding  $E$  mode intensity, with  $E$  mode polarization rods. **Bottom Left:**  $E$  and  $B$  modes defined about a center point.  $E$  modes are curl-free and are invariant under a parity transformation about the center point.  $B$  modes are divergence-free and are odd under parity transformations about the center point. **Bottom Right:** A map of the  $B$  mode intensity and  $B$  mode polarization rods corresponding to the top-left temperature map. Image from the Task Force on Cosmic Microwave Background Research [4]

$E$  and  $B$  modes draw their names from their parity properties, after the parity properties of multipole radiation. For  $l = 2$ , electric multipole radiation is even under parity, giving the even  $E$  modes their name. With  $l = 2$ , magnetic multipole radiation is odd under parity, thus naming the  $B$  modes.

Aside from their usefulness in allowing us to define polarization on a sphere,  $E$  and  $B$  modes are useful in categorizing the source of polarization of the CMB. As mentioned before, only two modes contribute the CMB polarization: scalar modes which represent density perturbations, and tensor modes which are gravitational waves. Scalar modes only produce  $E$  modes, whereas tensor modes produce both  $E$  and  $B$  modes. So, by observing CMB  $B$  mode polarization we can directly observe the effects of gravitational waves at the surface of last scattering and during reionization (neglecting foreground and lensing effects to be discussed in section 2.2).

$E$  and  $B$  modes are described by their power spectra in the same way as temperature fluctuations. We can also describe cross-correlation spectra by averaging two quantities together. We expect the  $TB$  and  $EB$  spectra to be zero, but the  $TE$  spectrum has been predicted and observed to be non-zero. We present a plot of the CMB  $BB$  power spectrum in the top portion of figure 2.1.

## 1.4 Inflation

While the  $\Lambda$ CDM model is broadly consistent with observation, there are a few peculiarities about the universe it fails to explain in a satisfying manner. These are the flatness problem, the horizon problem, and the monopole problem. To explain these observations the theory of Inflation was developed, first put forward by Alan Guth in 1981 [12].

Inflation is the theory that very early after the big bang ( $t \lesssim 10^{-34}$  s) the universe expanded exponentially, before stopping and continuing to grow according to standard cosmological models.

### 1.4.1 Problems in $\Lambda$ CDM

#### Flatness problem

The flatness problem is the problem that on very large scales, the universe appears to be nearly flat, or described by Euclidean geometry. More information about the curvature of the universe can be found in Appendix C.

Results from the 9-year WMAP observations have measured  $\Omega_0$  (the present value of  $\Omega(t)$ , the density parameter, which is a measure of the total energy density and shape of the universe) to great precision at [15]

$$1 - \Omega_0 = -0.0027^{+0.0039}_{-0.0038} \quad (1.4.1)$$

which is consistent with a flat universe ( $\Omega_0 = 1$ ). Even the most conservative estimates of the density parameter place

$$|1 - \Omega_0| \leq 0.2 \quad (1.4.2)$$

which is again consistent with a flat universe. While this value isn't abnormally close to a flat universe, it has grown with time. If these conservative limits are extrapolated back the value of the density parameter at the Planck time,  $t_P \sim 10^{-44}$  sec, we see

$$|1 - \Omega_P| \lesssim 10^{-60} \quad (1.4.3)$$

So, for present conditions of the universe, the density parameter must be fine tuned to one part

in  $10^{60}$  [32]. In the standard cosmological model one must accept this incredible precision without explanation. The theory of inflation provides a physical mechanism to smooth out the universe, and explain its flatness.

## Horizon Problem

The horizon problem is the problem that on very large scales the universe appears homogeneous and isotropic. While, in terms of the cosmological principle, it is certainly convenient that it does, it is nevertheless puzzling as there is no physical mechanism in  $\Lambda$ CDM cosmology that forces it.

To put it mathematically, we have observed that the CMB, which originates from the surface of last scattering is isotropic to within 1 part in 100,000. However, last scattering surface is very close to the horizon distance, the farthest distance light could travel given the age of the universe. As such, it takes a time almost equal to the age of the universe for light to reach us from this surface. This means that there is certainly not enough time for light from one side of the last scattering surface to have reached the other. Thus they are out of causal contact, and no information could be exchanged between the two sides. Yet, they are almost exactly the same temperature.

In fact, points on the last scattering surface that are separated by an angular distance of  $\theta \approx 2^\circ$  were out of causal contact with one another, and the CMB has no reason to be so homogenous. This homogeneity suggests that there is an additional mechanism beyond the standard cosmological model forcing these regions into causal contact [32].

## Monopole Problem

The monopole problem is the apparent lack of magnetic monopoles in the universe. Theories of high-energy physics argue that at sufficiently high energies the electromagnetic, weak, and strong forces unite to become a single Grand Unified Theory (GUT). It is predicted that this occurs around energy scales of approximately  $10^{12}$  TeV, corresponding to roughly  $t_{GUT} = 10^{-36}$  s after the big bang. At lower energies,  $\sim 1$  TeV ( $t_{ew} = 10^{-12}$  s), the electromagnetic and weak forces unite to form the electroweak force. When the energy level of the universe crosses the boundaries between the GUT energy scale, the electroweak energy scale, and the energy scale in which all three forces are distinct, the universe is said to undergo a phase transition.

These phase transitions are expected to give rise to certain topological defects. For the GUT to electroweak phase transition, it is expected that magnetic monopoles would be created. Not only would they be created, they would be created with a large enough energy density that at  $t \sim 10^{-16}$  s they would be the dominant component of the universe.

The problem, then, is that no magnetic monopole has been found and there is no strong evidence they even exist [32].

### 1.4.2 Inflation Solution

Inflation is a general paradigm for which many specific theories exist. The general idea is that in the early universe, there was a period of time during which the universe expanded exponentially with scale factor

$$a(t) \propto e^{H_i t} \quad (1.4.4)$$

After some time, this expansion was switched off, and the universe continued to evolve under standard cosmological theories. It is believed that inflation lasted until around  $10^{-34}$  s after the big bang. During the inflationary period, the universe expands faster than the speed of light, but its energy density remains relatively constant. Inflation is often described as causing the universe to undergo  $N$   $e$ -foldings, which means that the scale factor (and size of the universe) grew as  $e^N$  [32].

How does this solve the problems discussed before? As for the flatness problem, inflation drives down the curvature of the universe. For any kind of curvature before inflation, the curvature after would be close to zero. Specifically, if inflation begins at  $t_i$  and ends at  $t_f$ , the curvature goes as

$$|1 - \Omega(t_f)| = e^{-2N} |1 - \Omega(t_i)| \quad (1.4.5)$$

Inflation then exponentially damps the curvature of the universe.

As for the horizon problem, inflation posits that the universe was relatively small before inflation, and relatively large after. Thus, regions that are out of causal contact after inflation would have been exponentially closer together before inflation. They could be in causal contact before inflation, if  $N$  is sufficiently large.

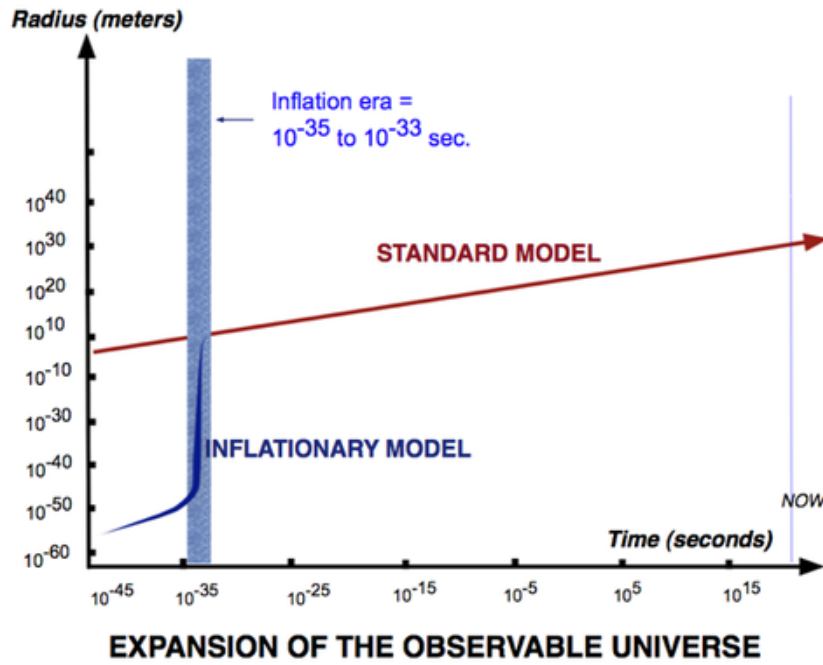


Figure 1.7: Size of the universe vs time under the standard cosmological model and the Inflation model. Under the standard model the size of the universe grew at a relatively constant rate since the Big Bang. Under Inflation, the universe grew exponentially within the first  $10^{-35}$  to  $10^{-33}$  sec before the standard model took hold. Image by Ethan Siegel [33]

As for the monopole problem, if magnetic monopoles were created before, or during inflation, their number density ( $n_M$ ) would be significantly damped by inflation as

$$n_M \propto e^{-3N} \quad (1.4.6)$$

Thus, even if monopoles were relatively abundant before inflation, they would be quite rare after.

Additionally, theories of inflation could explain the anisotropies in the CMB. Under inflation, the universe began with a size on quantum scales. The Heisenberg uncertainty principle dictates there would be quantum fluctuations in this early universe. Inflation would then grow these fluctuations and convert them into the density anisotropies observed on the surface of last scattering, which eventually grew into the structure observed in the universe [8].

For more information on inflation, including specific theories of inflation, see Clesse's *An introduction to inflation after Planck: From theory to observations* [8].

### 1.4.3 Inflationary observables

It is predicted that inflation will produce a gravitational wave background [4]. The amplitude of the gravitational waves is related to the energy scale of inflation. As such, observing the gravitational wave background would provide a measurement of that energy scale. These gravitational waves are characterized by their amplitude which is described by the tensor to scalar ratio  $r$ . This gives the ratio between the amplitude of the gravitational waves and the size of density perturbations at  $l = 2$ , a result which is constrained by the tensor contribution to the temperature power spectrum. Current data from BICEP2/Keck Array and Planck satellite give an upper limit of  $r < 0.12$  at the 90% confidence level [1].

These gravitational waves will produce a polarization pattern in the CMB. They are tensor modes and produce  $B$  mode polarization, which, in theory, could be measured. The  $BB$  power spectrum of the CMB will have two peaks produced from these waves. There will be a peak at  $l \sim 100$  produced from CMB polarization at the last scattering surface, and another at  $l \sim 6$  which is polarization generated after reionization. An observation of the  $BB$  power spectrum with these peaks will constitute a measurement of  $r$  and thus give the energy scale of inflation.

# Chapter 2

## Cosmology Large Angular Scale Surveyor (CLASS)

The Cosmology Large Angular Scale Surveyor (CLASS) is an experiment led by Dr Charles Bennett and Dr Tobias Marriage from Johns Hopkins University in collaboration with scientists at NASA Goddard. The CLASS experiment is a series of four telescopes which aims to observe the polarization of the CMB on large angular scales (low  $l$ ), by observing large fractions of the sky. By targeting large angular scales it is uniquely positioned to observe the expected reionization bump in the  $BB$  power spectrum, where the signal from inflationary gravitational waves is expected to dominate over a gravitational lensing foreground. The first telescope was deployed in late 2015 and observed its first light in May of 2016. The other telescopes are expected to follow shortly after and aim to collect data over a period of several years.

The CLASS telescopes have been designed to measure or place upper limits on the tensor to scalar ratio at a level of  $r = 0.01$ . The experiment will also be able to measure the optical depth <sup>1</sup> to the surface of last scattering with greater precision than current results [10].

---

<sup>1</sup>related to redshift

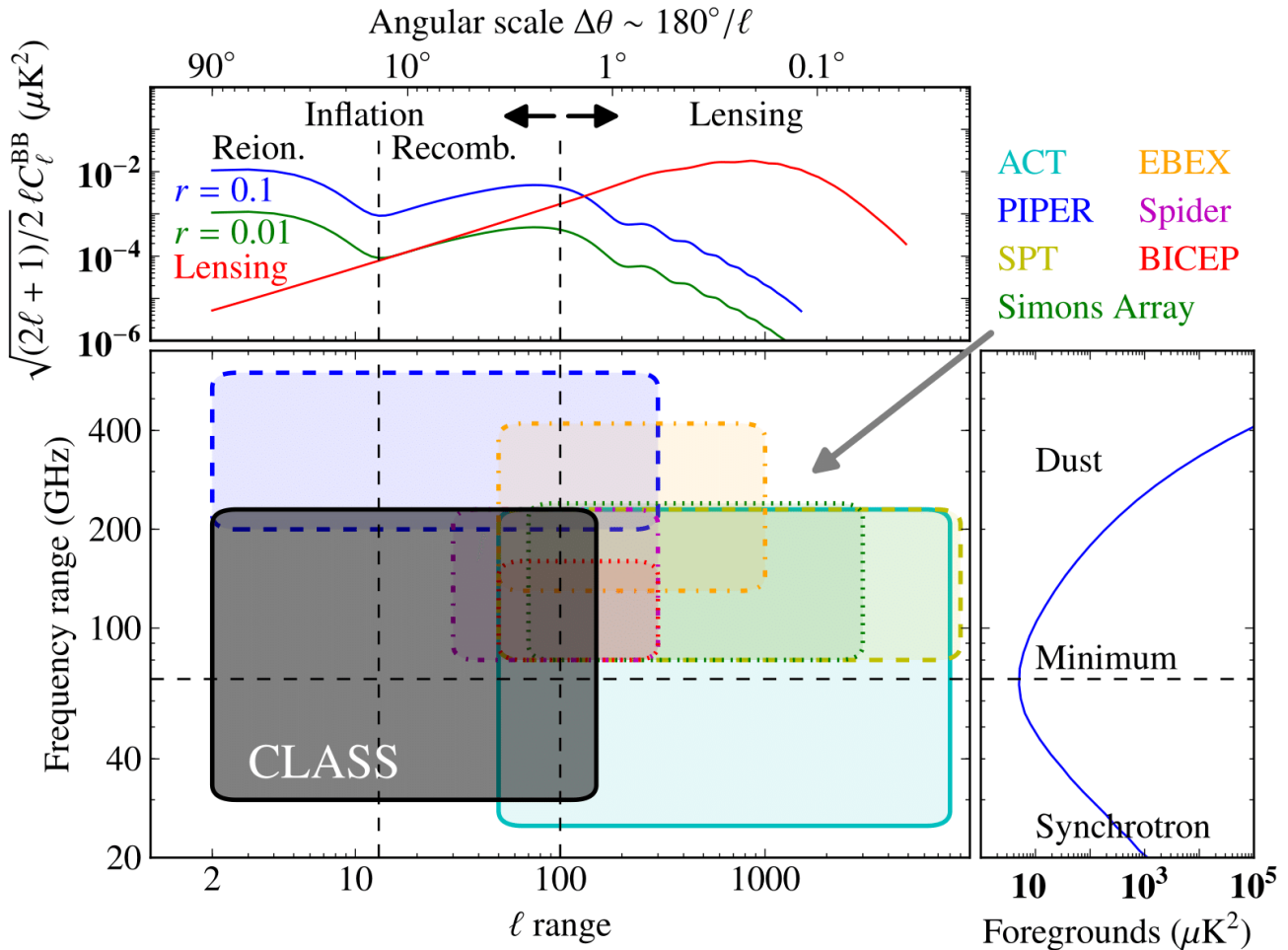


Figure 2.1: The CLASS search area. **Center:** The CLASS survey space (black box) plotted in frequency and multipole  $l$ . Other CMB experiments' surveys are featured in other colors. **Above:** The expected CMB  $BB$  power spectrum plotted against multipole and angular scale. The green and blue curves represent the inflationary gravitational wave signature for different values of the tensor to scalar ratio. The red curve represents the gravitational lensing signal. CLASS is positioned to target the reionization bump at large angular scales, where the inflationary signal dominates over the lensing foreground. **Right:** A plot of the galactic foregrounds against frequency. At low frequencies, the foreground signal is dominated by synchrotron radiation. At high frequencies it is dominated by thermal emission from dust. The CLASS experiment observes in a frequency range about the minimum in these foregrounds, while featuring a wide enough frequency range to distinguish CMB signal from the foreground. Image from Watts et al [35]

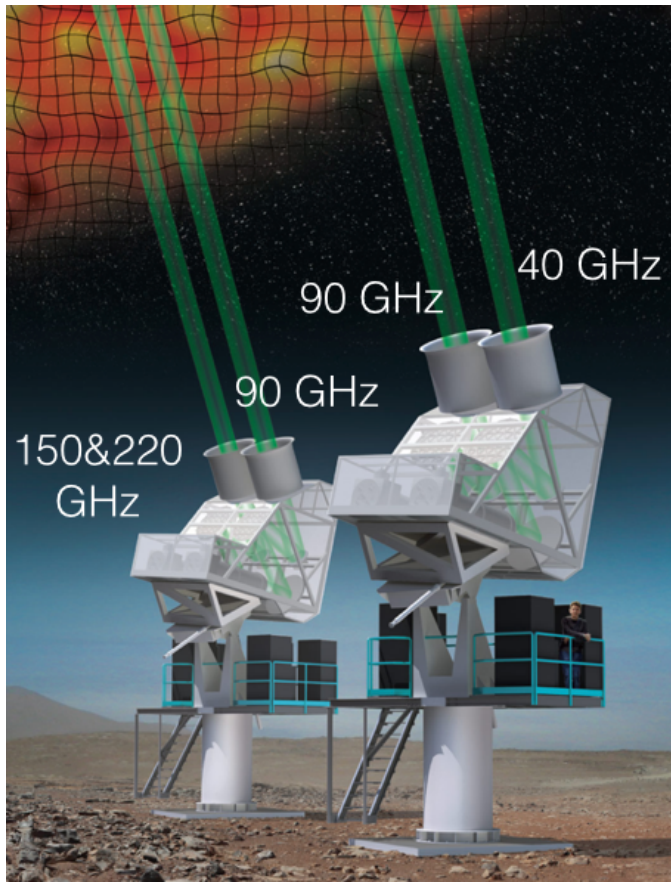


Figure 2.2: An artists rendition of the CLASS experiment. CLASS features four telescopes, observing at roughly the frequencies depicted, placed on two mounts. The telescopes will be deployed in the Atacama desert in Chile. Image from Essinger-Hileman et al [10]

## 2.1 Experimental Details

CLASS features four telescopes referred to as the Q, W1, W2 and HF(high frequency) band instruments. The Q band telescope is centered around a frequency of 38 GHz, the W band telescopes at 93 GHz and the HF telescope will feature a receiver with two bands centered at 148 and 217 GHz. The HF instruments are referred to as HF150 and HF220 respectively. These telescopes are deployed on two mounts with the Q and W1 sharing a mount, and the W2 and HF instruments sharing the second mount.

Each mount will perform constant elevation scans over a full  $360^\circ$  in azimuth<sup>2</sup> at a rate of roughly  $1^\circ$  per second. The telescopes will rotate  $15^\circ$  in boresight<sup>3</sup> once per day. The boresight rotations allow observations of a different polarization direction on the sky. This scan strategy will

<sup>2</sup>rotations about an axis perpendicular to the ground

<sup>3</sup>rotations about the telescopes beam axis

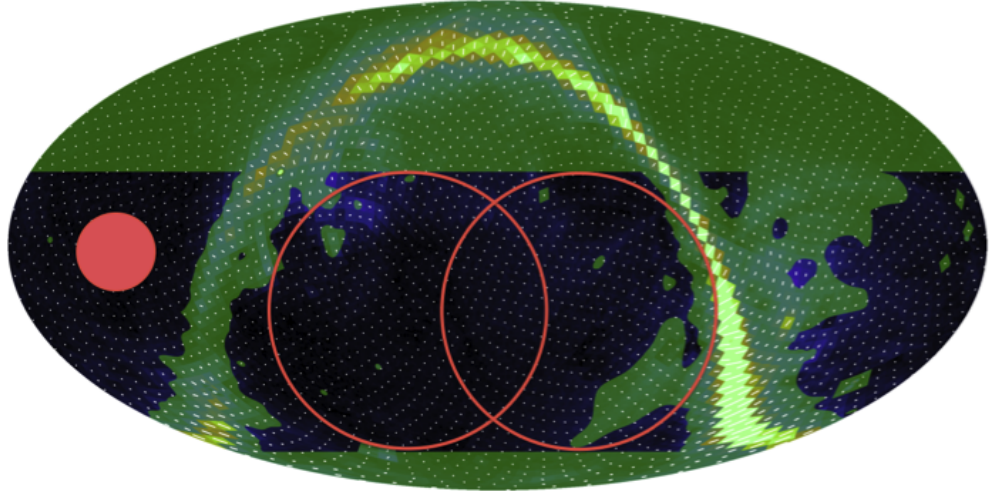


Figure 2.3: The CLASS search strategy on a simulated map of the sky. The experiment will cover about 70% of the sky every day. The portions of the image masked in green are regions the CLASS telescope will not include for data analysis. The small red filled circle marks the instantaneous field of view of one telescope. The large circles denote the area covered by one full rotation of the telescope. Image from Essinger-Hileman et al [10]

cover about 70% of the sky every day. Portions of the sky corresponding to the galactic equator will be cut out as shown in figure 2.3, giving CLASS a final sky fraction of about 50% [35]. This survey of a large portion of the sky allows for observations at low multipole  $l$ .

The telescopes will be placed in the Atacama desert in Chile. This area is a desert featuring a particularly dry climate which reduces atmospheric foregrounds. It also features a relatively low latitude at  $-23^\circ$  allowing observation of a large portion of the sky.

## 2.2 Foregrounds

The CLASS frequency bands were chosen to be simultaneously around the minima in galactic foregrounds and at minima in atmospheric absorption. The galactic foreground is largely dominated by synchrotron emission at low frequencies and thermal dust emission at high frequencies. Both effects produce B mode polarizations and contribute noise to the CLASS experiment. The galactic foreground reaches its minimum around  $\sim 70$  GHz [18]. Atmospheric absorption in the frequency range of interest is dominated by oxygen and water vapor, and prohibits observations around these absorption frequencies. These constraints motivate the choice of the CLASS frequency bands.

Atmospheric absorption lines are shown in figure 2.4, along with the CLASS bands. These lines

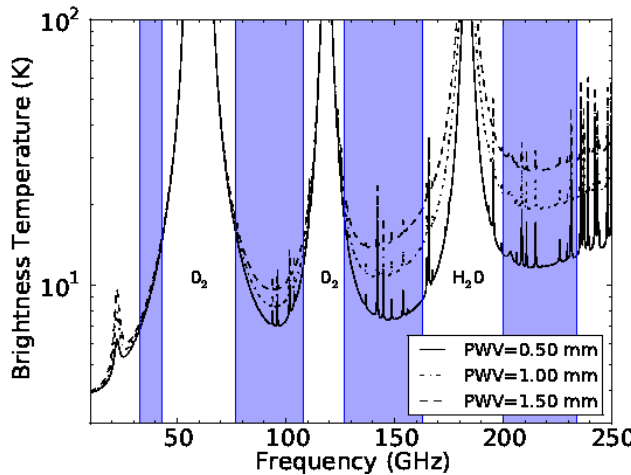


Figure 2.4: Atmospheric absorption lines measured in brightness temperature vs frequency for a given precipitable water vapor (PWV). High brightness temperature prohibits observation for a given frequency. The CLASS frequency bands are shown in blue, chosen to correspond to minima in this spectrum. The CLASS site in the Atacama desert has a yearly median PWV of 1.3 mm. Image from Essinger-Hileman et al [10]

are strongly dependent on the moisture content of the air as measured in mm precipitable water vapor (PWV)<sup>4</sup>, motivating the choice of a dry environment like the Atacama desert for the CLASS site. For the Atacama desert, the yearly median PWV is 1.3 mm [10].

Synchrotron emission is a result of cosmic ray electrons traveling through magnetic fields in the galaxy. This process releases a polarized photon which constitutes noise for CMB polarization experiments. Thermal dust emission is thermal radiation from interstellar dust. For asymmetric shapes of dust, this radiation can be polarized. Observations by WMAP and Planck have measured these sources [18].

CLASS is set up to be able to remove foreground sources in its measurements. The Q band telescope will measure synchrotron sources, and the HF220 will measure dust sources. The results from these observations can be used to remove foreground noise in the primary CMB channels: W1, W2 and HF150. Considering the galactic foregrounds, CLASS is projected to have a sensitivity of 10  $\mu\text{K-arcmin}$  in the W channels. This allows the experiment to place an upper limit on the tensor to scalar ratio of  $r = 0.008$  at a 95% confidence level when considering a full range of multipoles [35].

<sup>4</sup>A measure of the amount of water in a column of air, if all that water were to precipitate

### 2.2.1 Lensing

A second source of foreground for CLASS measurements of inflationary gravitational waves is gravitational lensing of CMB photons. This contributes to the  $BB$  power spectrum as seen by the red line in the top section of figure 2.1. While this prohibits detection of inflationary gravitational waves on small angular scales, detailed measurements of galactic lensing can inform other cosmological parameters and is not considered foreground for all experiments. It has been observed in detail by the South Pole Telescope and other experiments [20].

The lensing signal in the  $BB$  power spectrum is a result of CMB  $E$  mode photons traveling through a gravitational field. A well known consequence of general relativity is that when light moves through a gravitational field its path curves. When observing a cosmic light source behind a large mass, the photons traveling directly to the observer are blocked by the mass. Those traveling at a slight angle to the observer are curved from the gravitational field of the mass and reach the observer. The result is the light source appears as a disk surrounding the intervening mass. For CMB photons, an intervening mass warps  $E$  modes into  $B$  modes, creating a  $B$  mode signal that is independent of inflationary gravitational waves.

The lensing signal dominates the  $BB$  spectrum at large multipoles ( $l \gtrsim 100$ ). The CLASS experiment is designed to target low multipoles so that it can observe the inflationary signal.

## 2.3 Optical Design

The optical design of each CLASS telescope consists of several ‘warm’ elements at ambient temperature and several ‘cold’ elements cooled by a cryostat to multiple stages. The design of the telescopes is sketched out in figure 2.5.

The warm elements in order are the variable-delay polarization modulator (VPM), and a primary and secondary mirror. The VPM is to be discussed in detail in chapter 3. It serves to reduce sources of systematic error by modulating incoming linear and circular polarization at a frequency of 10Hz. The primary and secondary mirrors are ellipsoid section shaped pieces of aluminum, each about 1.5 m in diameter.

An ultra high molecular weight polyethylene (UHMWPE) window treated with anti-reflective

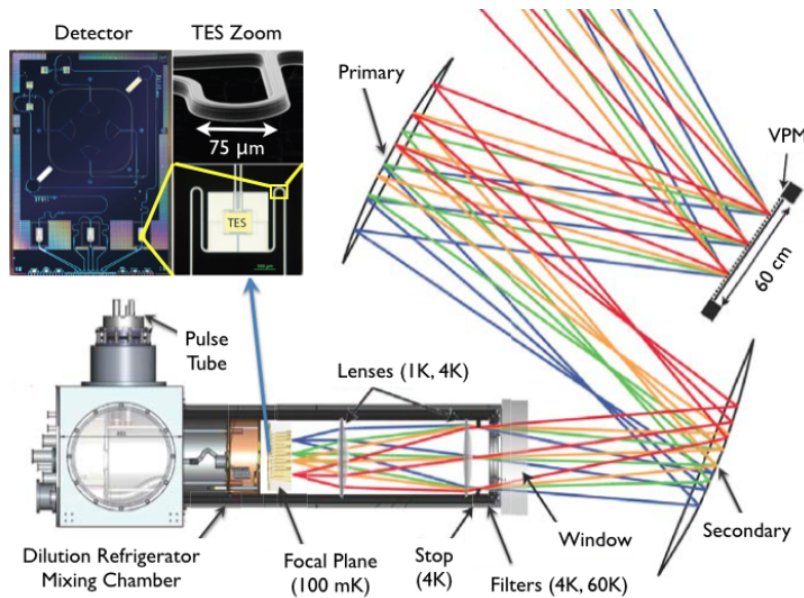


Figure 2.5: The CLASS optical design. The first element is the VPM which modulates incoming polarization and reduces systematics. Light is directed through the optical elements depicted into a cryostat and onto a focal plane of detectors at 100mK. An image of a Q band detector and close up of a TES bolometer are included. Image from Essinger-Hileman et al [10]

(AR) coating serves as the entrance to the cryostat. It covers the 46 cm opening to the cryostat and holds a vacuum inside. The material was chosen as it is transparent to the microwave frequencies of interest. Inside the cryostat, the first elements are 60K and 4K infrared filters. These limit the amount of infrared radiation that reaches the detectors and reduce thermal noise. There are two filter designs: metal mesh filters which reflect infrared wavelengths and transmit microwaves, and AR coated polytetrafluoroethylene (PTFE) filters which absorb infrared wavelengths. A cold aperture stop at 4K controls the telescopes field of view. After the cold stop there are two lenses positioned at the 4K and 1K stages which direct the light onto a focal plane. For the Q and W band instruments, these are high-density polyethylene which does not significantly absorb at those frequencies. For the HF instruments, silicon lenses will be used for their superior transmittance at higher frequencies. The focal plane consists of an array of feedhorns which focus light directly onto the detectors.

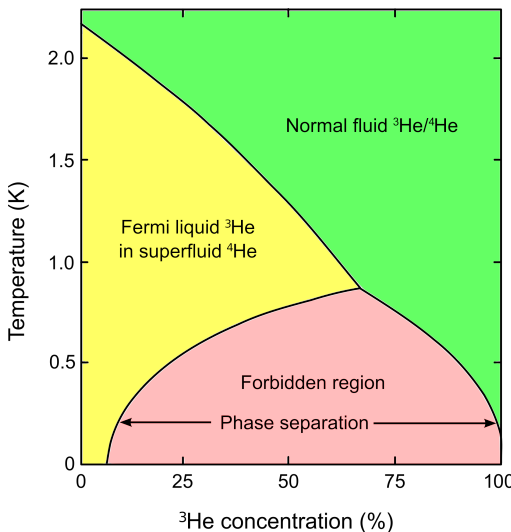


Figure 2.6: A phase diagram for low temperature  $^3\text{He}/^4\text{He}$  mixtures. Below a critical temperature the mixture separates into an  $^3\text{He}$  rich fluid and an  $^3\text{He}$  poor superfluid. In a dilution refrigerator, the  $^3\text{He}$  equilibrium is disturbed and energy is required to make the phase transition to restore it. The energy is drawn from an external source, cooling that source [26].

### 2.3.1 Cryostat

Each CLASS cryostat was designed by BlueFors Cryogenics<sup>5</sup>. They are made specially to be able to function horizontally and provide a large volume cooled to 4K. They are magnetically shielded to protect magnetically sensitive amplifiers and detectors. The primary cooling power on the focal plane comes from a  $^3\text{He}/^4\text{He}$  dilution refrigerator. Such a device uses the heat of mixing of the helium isotopes to achieve temperatures of 100mK and below.

At sufficiently low temperatures, a mixture of  $^3\text{He}$  and  $^4\text{He}$  isotopes undergoes a phase separation into a normal fluid with a high concentration of  $^3\text{He}$  (rich) and a superfluid with a low concentration (poor) as seen in figure 2.6.  $^3\text{He}$  is then pumped in through the rich fluid and out through the poor fluid, destroying the equilibrium. To restore the equilibrium, the  $^3\text{He}$  wants to move from the rich fluid to the poor [3]. Doing so requires energy, which for the CLASS cryostats is drawn from the focal plane. This process cools the focal plane to roughly 100mK.

The initial cooling for the dilution refrigerators comes from pulse-tube cryocoolers. A standard Stirling cryocooler cools gasses through adiabatic expansion. Ambient temperature air is compressed isothermally and enters a regenerator. The regenerator takes heat from the gas, and the far side

<sup>5</sup>BlueFors Cryogenics, Arinatie 10, 00370 Helsinki, Finland; <http://www.bluefors.com/>

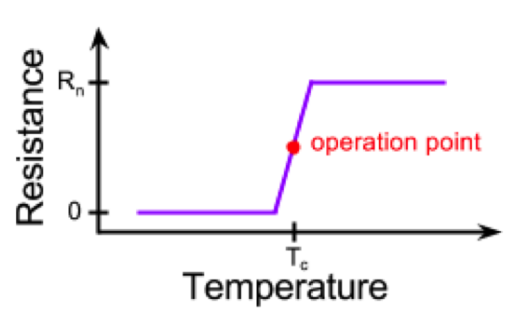


Figure 2.7: A sketch of the resistance/temperature relation for a transition edge sensor. The sensor is held at the operation point in red. Here the resistance is very sensitive to temperature so that small change in temperature triggers a measurable change in resistance. Image by Lindsay Lowry [24]

is at a lower temperature. The gas on the far side is expanded isothermally taking heat from its surroundings. The system then returns to its initial state by moving the gas back through the regenerator while maintaining a constant volume. A pulse-tube cryocooler achieves a similar cycle without any moving parts at the cold end [31]. These are put in stages to provide multiple stages of cooling.

The CLASS cryostats feature temperature stages of 60K, 4K, 1K, and 100mK.

### 2.3.2 Detectors

The focal plane feedhorns feature an ortho-mode transducer at their base to separate orthogonal linear polarization components. Each polarization state is then measured by separate transition edge sensor (TES) bolometers.

TES bolometers feature a superconducting material held at its critical temperature. Around the critical temperature, the sensor's resistance is very sensitive to changes in temperature as sketched in figure 2.7. CMB photons incident on the TES bolometers will cause a small temperature change that triggers a measurable change in resistance. The CLASS detectors have transition temperatures around 150mK. The low temperature means that there is low thermal noise on the detectors. The detectors were produced at NASA Goddard.

The signal from a detector is then amplified by an array of superconducting quantum interference devices (SQUIDs) at 4K before being read out by room temperature electronics.

# Chapter 3

## Variable-Delay Polarization Modulator

The first optical element in each CLASS telescope is a variable-delay polarization modulator (VPM). This functions to modulate the incoming polarization signal while not affecting the unpolarized component. By placing it as the very first optical element, it is able to modulate signal polarization without affecting instrumental polarization. Thus, the CLASS telescopes are able to effectively distinguish between polarization from the sky, and noise introduced from both unpolarized light and instrumental polarization. In addition, the CLASS VPMs function as fast polarization modulators allowing the experiment to limit  $1/f$  noise contributions from the atmosphere.

The VPM consists of a wire grid placed before a translating mirror driven at a frequency of 10 Hz. The wire grid is a collection of parallel metal wires evenly spaced which functions to reflect one incoming polarization state and transmit an orthogonal polarization state. The mirror is moved such that it always parallel to the wire grid. Its function is to introduce a phase difference between polarization components reflected or transmitted by the wire grid.

### 3.1 Operation

In this section we describe the function of the VPM in detail. First we define the  $\hat{y}$  axis as being along the wires in the wire grid, and the  $\hat{x}$  axis as perpendicular to the wires. Then, suppose the telescope is oriented such that  $Q$  polarization states on the sky are aligned with the  $\hat{x}$  and  $\hat{y}$  axes, and  $U$  polarization on the sky is  $45^\circ$  to the axes.

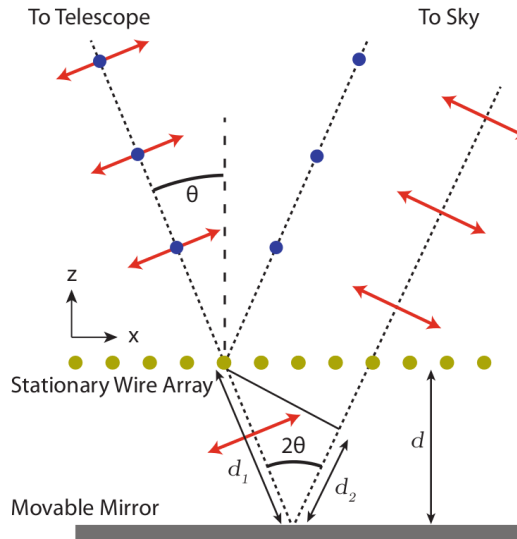


Figure 3.1: A sketch of the VPM. Incident light (dotted line) features two orthogonal polarization components denoted by red arrows and blue dots. The wire grid (gold dots) will reflect polarization parallel to the wires and transmit perpendicular polarization. As the transmitted polarization travels farther it picks up a phase difference  $\phi$  relative to the reflected component. When the distance between the mirror and the wire grid is varied,  $\phi$  varies and the incoming polarization is modulated.

First we consider incoming  $Q$  polarization states. If the incoming  $Q$  is in the  $\hat{y}$  direction, it is entirely reflected by the wire grid. If it is in the  $\hat{x}$  direction, it is entirely transmitted and picks up an overall phase factor, which is unimportant. The detectors will then see the full  $Q$  state, functionally unaffected by the VPM.

Now consider incoming  $U$  polarization. The polarization is aligned  $45^\circ$  to the axes and will have  $x$  and  $y$  components. The  $y$  component will be reflected by the wire grid, while the  $x$  axis will be transmitted. Thus, the  $x$  component picks up a relative phase difference of  $\phi = 2kd \cos \theta$ <sup>1</sup> where  $k$  is the wavenumber of the incoming light,  $d$  is the VPM mirror-grid separation distance, and  $\theta$  is the angle of the incoming light relative to the  $\hat{z}$  axis. Because of the relative phase difference, the polarization state on the detector, which is the sum of the reflected and transmitted polarization states, changes. For incoming  $+U$  polarized light and given relative phase differences  $\phi$ , the polarization received by the detector is summarized in table 3.1.

<sup>1</sup>The mirror translates during this time so in reality the phase difference is  $\phi = k \cos \theta(d_i + d_r)$  where  $d_i$  and  $d_r$  represent the mirror-grid separation for incoming and reflected light. Since light travels much faster than the VPM distance changes, we can safely approximate  $d_i = d_r$ .

Table 3.1: Observed polarization state on a detector for incoming  $+U$  polarization modulated by a VPM.

$\phi$	Observed Polarization
0	$+U$
$\pi/2$	$+V$
$\pi$	$-U$
$3\pi/2$	$-V$
$2\pi$	$+U$

The VPM introduces a relative phase difference  $\phi$  between orthogonal components of the incoming polarization which changes the polarization state observed

Table 3.1 describes the polarization state on a detector for a given incoming polarization state. In reality there are several polarization states on the sky and the detector only picks up one. If we consider, instead, the  $+U$  polarization state coming from the detector, the same analysis will apply and the polarization on the sky can be given by table 3.1. Thus, a single CLASS detector can observe the entire  $U$  and  $V$  polarization on the sky. If the telescope is then rotated  $45^\circ$  in boresight, it will observe the entire  $Q$  and  $V$  polarization on the sky.

### 3.1.1 Mathematical Interpretation

Here we will describe the operation of a CLASS VPM mathematically in terms of Jones matrices and Stokes parameters. We use Joseph Eimer's thesis as a reference [9]. See Appendix A for more on these topics. The light reflected from the VPM is the coherent sum of the light that is reflected from the wire grid, and that which is transmitted and reflected off of the mirror. The Jones matrices for these elements are listed in Table 3.2. Let the wire grid be aligned such that the  $\hat{y}$  polarization state is reflected and the  $\hat{x}$  polarization state is transmitted, as before. We can then write Jones matrix for the entire VPM system as:

$$J_{VPM} = J_{WR\hat{y}} + J_{WT\hat{x}} \cdot J_{trans}(d_2) \cdot J_{mirror} \cdot J_{trans}(d_1) \cdot J_{WT\hat{x}} \quad (3.1.1)$$

$$= \begin{pmatrix} e^{i2kd \cos \theta} & 0 \\ 0 & -1 \end{pmatrix} \quad (3.1.2)$$

Table 3.2: Jones matrices for VPM and telescope optical elements

Optical element	Notation	Jones matrix
Wire grid polarizer reflecting $\hat{y}$ polarization	$J_{WR\hat{y}}$	$\begin{pmatrix} 0 & 0 \\ 0 & -1 \end{pmatrix}$
Wire grid polarizer transmitting $\hat{x}$ polarization	$J_{WT\hat{x}}$	$\begin{pmatrix} 1 & 0 \\ 0 & 0 \end{pmatrix}$
Travel of wave with wavenumber $k$ through distance $d$	$J_{trans}(d)$	$\begin{pmatrix} e^{ikd} & 0 \\ 0 & e^{-ikd} \end{pmatrix}$
Reflection from mirror	$J_{mirror}$	$\begin{pmatrix} 1 & 0 \\ 0 & -1 \end{pmatrix}$
Rotation through angle $\alpha$	$J_R(\alpha)$	$\begin{pmatrix} \cos \alpha & -\sin \alpha \\ \sin \alpha & \cos \alpha \end{pmatrix}$

Where  $d$  is the wire-grid mirror separation and  $\theta$  is the angle of the incident light relative to the wire grid plane. To account for the complete optical system we must include elements representing the primary and secondary mirrors and a detector rotated at a general angle  $\alpha$  to the  $\hat{x}$  axis. Thus the Jones matrix for the light incident on the detector is:

$$J_{det} = J_{VPM} \cdot J_{mirror} \cdot J_{mirror} \cdot J_R(\alpha) \quad (3.1.3)$$

$$= \begin{pmatrix} e^{i2kd \cos \theta} \cos^2 \alpha & \cos \alpha \sin \alpha \\ -e^{i2kd \cos \theta} \cos \alpha \sin \alpha & -\sin^2 \alpha \end{pmatrix} \quad (3.1.4)$$

To find the power incident on a detector, we transform  $J_{det}$  to its corresponding Mueller matrix and take the dot product of the top row with the Stokes vector describing incident light ( $I, Q, U, V$ ) (See Eugene Hecht *Optics* [14]). The resultant power is:

$$P_{det}^{MC} = \frac{g}{2}(I + Q \cos 2\alpha + \sin(2\alpha)[U \cos(2kd \cos \theta) + V \sin(2kd \cos \theta)]) \quad (3.1.5)$$

where we have multiplied by the gain of the detector. This is the correct result for monochromatic light, hence the superscript. For a range of frequencies, we multiply  $P$  by the bandpass  $B(k)$  and integrate over all frequencies:

$$P_{det} = \frac{g}{2} \int_0^\infty dk(I + Q \cos 2\alpha + \sin(2\alpha)[U \cos(2kd \cos \theta) + V \sin(2kd \cos \theta)])B(k) \quad (3.1.6)$$

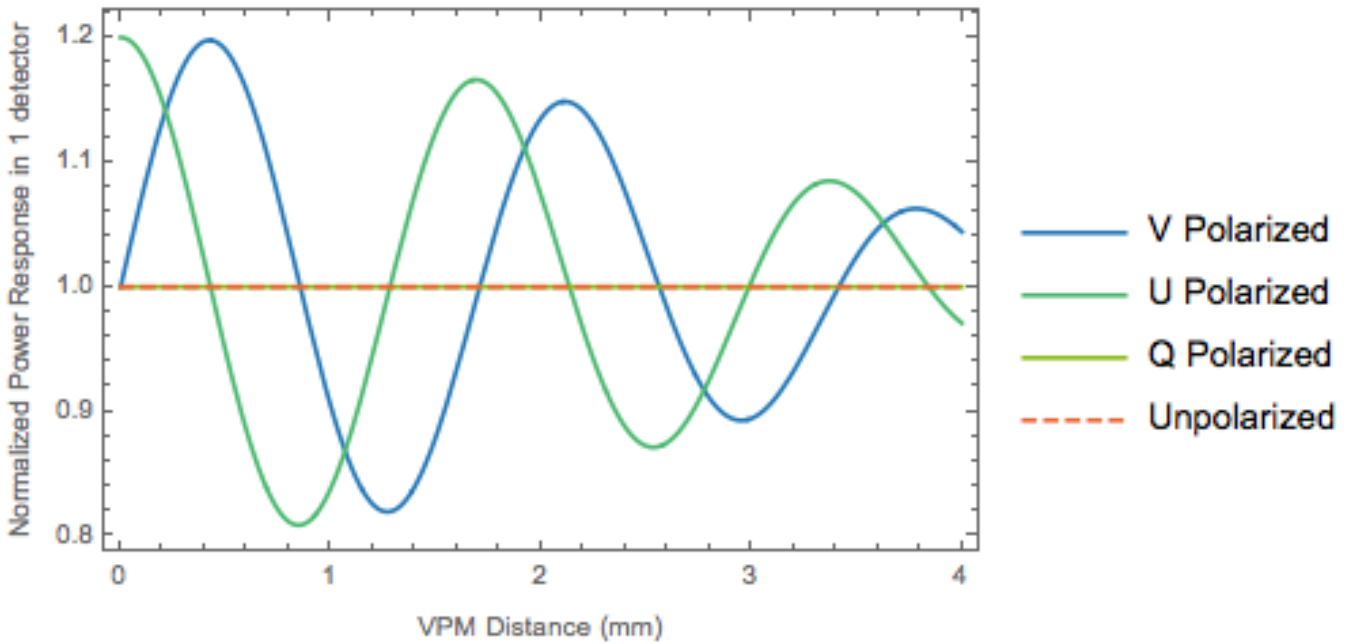


Figure 3.2: The power received in one detector plotted against VPM mirror to grid distances for a CLASS W band VPM for different incoming polarization components. We can see that the VPM modulates incoming Stokes  $U$  and  $V$  parameters, and leaves  $I$  (unpolarized) and  $Q$  unchanged.

The signal is maximized for  $\alpha = 45^\circ$ , and so the CLASS detectors are all oriented at  $45 \pm 3^\circ$  from  $\hat{x}$ . For a gain of 1,  $\alpha = 45^\circ$  and a perfect bandpass from 77-108 GHz representing one of the CLASS W band receivers, we can evaluate equation 3.1.6 for varying polarization states of incoming light. For a VPM mirror to grid distance from 0 to 4 mm and incoming light with a single polarization component, the result is plotted in figure 3.2. We can see that the CLASS optical system modulates incoming  $U$  and  $V$  polarizations while not affecting incoming  $I$  and  $Q$  parameters.

To observe an entire period of the modulated signal, the VPM travel distance must capture at least a full half-wavelength of the oscillations. To capture the full  $U$  modulation then, the W band VPM has a desired travel from  $d \sim 0.8\text{mm}$  to  $d \sim 1.8\text{mm}$ . A detailed optimization of the VPM travel was performed in [25] and for a sinusoidal travel, the mirror to grid distance will vary from  $d = 0.80$  to  $d = 1.81$  mm.

## 3.2 Benefits

CLASS VPMs work in several ways to reduce systematic error on polarization measurements. As discussed above, the VPM will modulate incoming polarized light while not affecting unpolarized light. The current measured by a single CLASS detector then consists of a DC component corresponding to the unpolarized light, and an AC component corresponding to the polarized light. Since the AC component oscillates at a known frequency (the driving frequency of the VPM, 10Hz), a bandpass filter can be applied to extract the polarized signal. Thus, each CLASS detector can completely measure a single linear stokes parameter.

A VPM is not the only polarization modulator that could be used for the CLASS telescope. The choice of a VPM for the polarization modulator was motivated by a desire to place the modulator as the first optical element. Unlike modulation techniques employing dielectric elements<sup>2</sup>, the VPM uses only reflective elements, and can be used at ambient temperature without a sensitivity loss. By placing the VPM as the first optical element in the telescope, it will modulate polarization from the sky but not polarization introduced from the instrument. Any polarization introduced by the instrument will contribute to the DC channel measured in the detector and can be removed the same way as with unpolarized signal.

The VPM modulates Stokes  $U$  and  $V$ . The  $V$  parameter for the CMB is expected to be zero, and so the VPM functions to switch ‘on’ and ‘off’ the  $U$  parameter in the detectors. Measuring the  $V$  parameter serves as a check for systematics in a null channel and can be used for calibration.

### 3.2.1 $1/f$ noise

By choosing a relatively fast driving frequency for the VPM of 10 Hz, the VPM is able to reduce the contribution of  $1/f$  noise from the atmosphere.  $1/f$  noise<sup>3</sup> is a phenomenon where noise goes as  $1/f^\alpha$  for  $\alpha \in (0, 2)$  up to a certain frequency,  $f_{knee}$ , also called the corner frequency. At frequencies above  $f_{knee}$  thermal noise takes over and the spectrum is constant. This phenomenon arises from low-frequency variations in the instrument and the environment [27]. A typical noise spectrum is given in figure 3.3.

---

<sup>2</sup>Such as a rotating half wave plate as used on the Atacama B-Mode Search [22].

<sup>3</sup>Also called pink noise or flicker noise in electronics

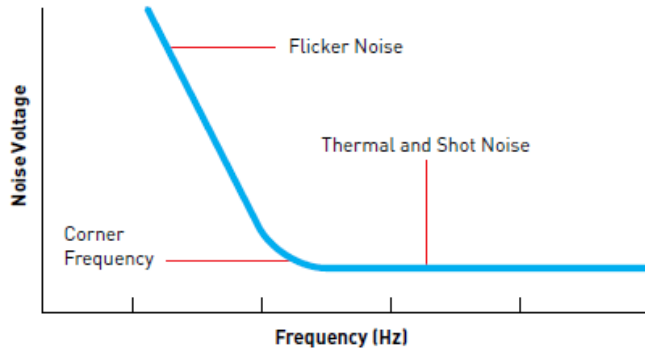


Figure 3.3: A typical noise spectrum featuring  $1/f$  noise (Also called flicker noise in electronics) and standard thermal noise. At low frequencies, below some corner frequency, noise goes as  $1/f^\alpha$  [13]

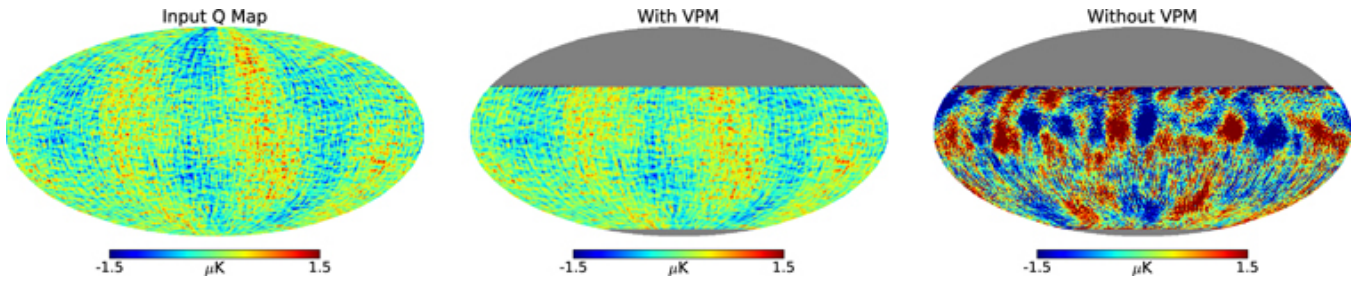


Figure 3.4: Recovered map of Stokes  $Q$  of the CMB for simulations with polarized  $1/f$  noise. The left map is the input map. The effect of the  $1/f$  noise can be observed by comparing the rightmost map to the input map. The effect of the VPM to reduce  $1/f$  noise can be seen in the middle map. The amplitude of the noise was arbitrarily chosen to demonstrate the effectiveness of the VPM. Image by Miller et. al. [27]

For the atmosphere,  $f_{knee} \approx 1\text{Hz}$  [22]. Since the CLASS VPMs modulate at a frequency above  $\approx 1\text{Hz}$ , the contributions from atmospheric  $1/f$  noise can be suppressed by placing a bandpass filter on the data. The effect of a VPM in reducing  $1/f$  noise on CMB polarization measurements has been simulated by Miller et. al. in [27], and is shown in figure 3.4.

$1/f$  noise is also introduced from instrumental variations. This noise contribution is reduced by thermally regulating the VPM and other warm optics inside a co-moving ground shield on the CLASS telescopes.

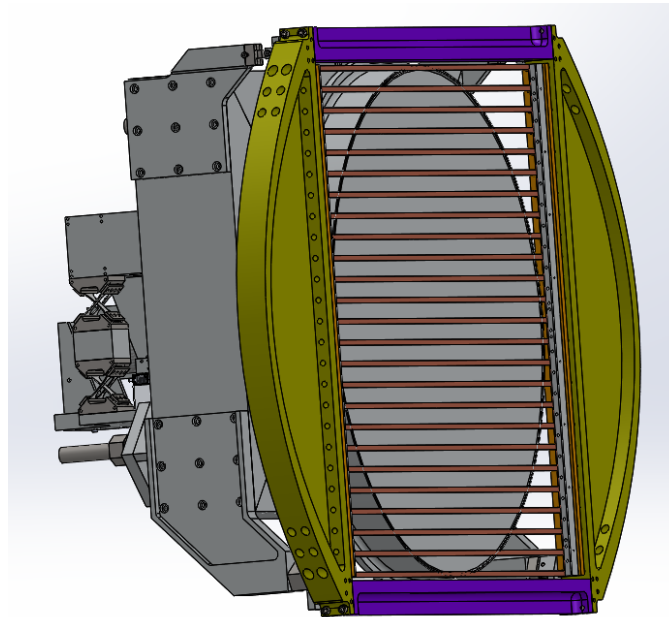


Figure 3.5: A rendering of a CLASS VPM. The spacing of the wire grid has been exaggerated to show the elements behind. The circular disk immediately behind the wires is the VPM mirror. Around the mirror is the counterweight system, and behind the counterweight the MTM can be seen with a single reaction axis flexure shown.

### 3.3 Design

The CLASS VPMs are specially designed to be able to confer the benefits discussed above. A rendering of a complete CLASS VPM is shown in figure 3.5. The VPM has been completed for the Q band telescope and a second is under construction for one of the W band telescopes.

In order to achieve the aforementioned benefits of the VPM, the wire grid must be an effective polarization isolator, and the mirror must be able to move a distance on the order of several millimeters, and oscillate at a high frequency (10Hz). In order to ensure the mirror and wire grid are pointed at the same section of the sky, they must maintain parallelism while the mirror translates. As such, the mirror cannot be allowed to tilt with respect to the wire grid. The system must operate without moving the entire telescope as the SQUID amplifiers are vibration sensors, and any disturbance to them will contribute noise to the data. The mechanism to translate the mirror is discussed in detail in chapter 4.

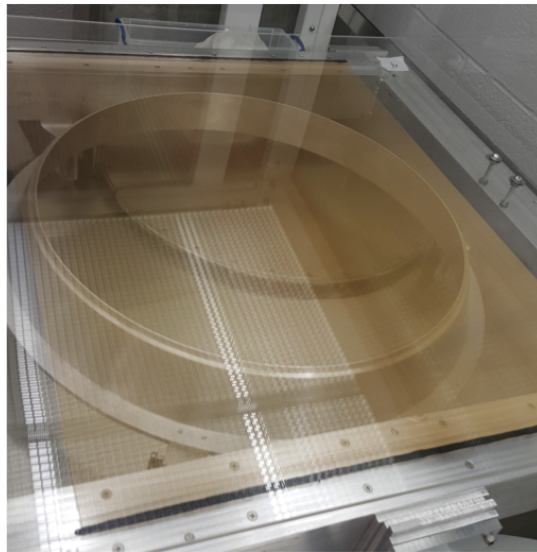


Figure 3.6: A CLASS VPM grid. The flattening ring can be seen underneath the wires, and the grid frame can be seen attached to them. Photo

### 3.3.1 Wire Grid

As the first VPM element the wire grid performs a crucial function in separating polarization states. For the VPM to function as intended, the grid wires must be highly reflective, parallel and similarly spaced. When these conditions are met, it has been shown that when the wavelength of light is significantly larger than the diameter of the grid wires, a VPM functions in close agreement with the model described earlier. That is, the VPM introduced phase delay is very nearly that given from only the grid mirror distance [7]. For the CLASS frequencies range, light will have wavelengths from  $\sim 1.3 - 7.5$  mm.

The material chosen for the CLASS VPMs is copper plated tungsten, to ensure high reflectance and that the wire can be placed under enough tension so that they aren't excited by the motion of air around them. The wires are chosen to have a diameter of 64  $\mu\text{m}$ , well below the wavelength of light, and a spacing of 200  $\mu\text{m}$ . A CLASS VPM wire grid is shown in figure 3.6 [9].

# Chapter 4

## Mirror Transport Mechanism

The mechanism used to translate the mirror is referred to as the mirror transport mechanism (MTM). It is designed to move the mirror with a high degree of parallelism relative to the grid while minimizing vibrations on rest of telescope. To maintain parallelism, the MTM element which holds the mirror is a planar four-bar linkage. This system uses a series of four flexures arranged in a rectangular pattern which can move the mirror linearly in one direction while preventing rotation or translation in others. The system is driven by a voice coil. A control system is in place to adjust the output of the voice coils and ensure optimal performance. For this system, position data is collected by way of linear encoders.

The mirror itself is a flat piece of honeycomb aluminum panelling. Such a panel is lightweight, and reflective to microwaves [9].

To prevent vibrations of the telescope, a counterweight is driven opposite the motion of the mirror such that the center of mass of the system remains constant. The structure holding the mirror is henceforth referred to as the mirror axis, and that holding the counterweight as the reaction axis. The reaction axis is designed in the same manner as the mirror axis with slight modifications for spacial constraints.

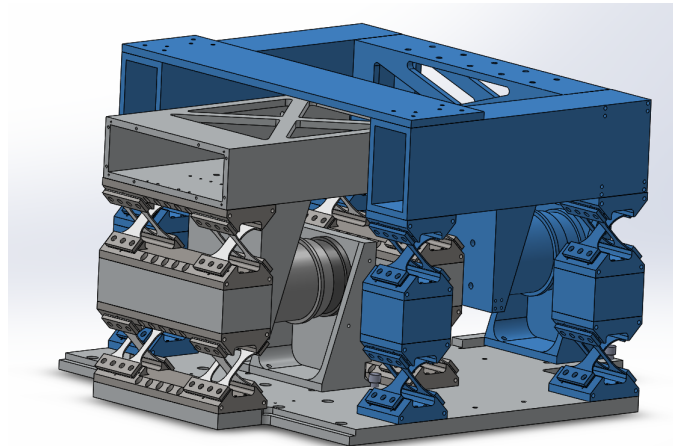


Figure 4.1: A rendering of the CLASS MTM. The mirror is attached to the grey structure and the counterweight to the blue. The flexure system for each axis can be seen in detail. The cylindrical objects shown are the voice-coils. Not pictured: the mirror, counterweight or linear encoders.

## 4.1 Flexures

The MTM mirror and reaction axis bodies are compliant mechanisms which transform the force input by the voice coils into linear translation of the mirror or counterweight by way of deforming an assembly of flexure hinges<sup>1</sup>.

A flexure strap is a flexible slender piece connecting two rigid bodies creating a hinge. The strap is designed to bend and allow the hinge to rotate. When bent the strap exerts a force on the bodies exactly analogous to a spring displaced from equilibrium. In this sense, flexure systems can be treated as spring systems and modeled by a spring constant  $k$ . By design, flexure hinges allow rotation in one direction but prohibit it in the other two<sup>2</sup>, and do so without any moving parts. Flexures can also function as load bearing structure elements.

Flexure hinges provide several advantages over traditional hinges. They suffer no friction losses, require no lubrication, and generally require no maintenance. They are however, more sensitive to changes in the environment, as thermal expansion and contraction of the strap will change its compliant properties. Typically they are only capable of providing a small degree of rotation [23].

The CLASS mirror and reaction axis flexure hinges consist of two spring steel flexure straps

<sup>1</sup>In the rest of this document a flexure assembly is referred to simply as a flexure. In this section we will take care to make it clear if we refer to a single flexure strap, a flexure hinge, or an assembly of hinges.

<sup>2</sup>There do exist two-axis flexures which can allow rotation in two dimensions. For the purposes of this document, we refer only to one-axis flexures

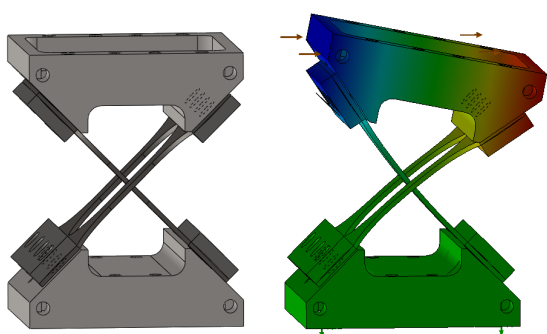


Figure 4.2: A flexure hinge. The design allows for rotation in the direction shown while constraining rotation in other directions.

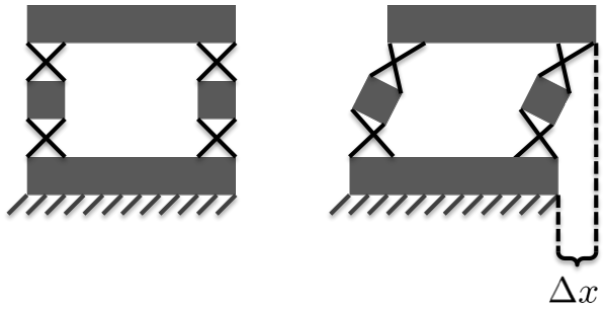


Figure 4.3: A four bar linkage made from flexure hinges. Such a system can move linearly right and left but cannot tilt up or down. A second four bar linkage constrains tilt and motion into and out of the page.

oriented perpendicularly to one another and  $45^\circ$  to the ridged bases, in an ‘X’ shape. A rendering of a class hinge is shown in figure 4.2. By utilizing two flexure straps on each hinge, the rotation along non-desirable axes is further constrained.

Each hinge in the MTM is coupled with another which is offset vertically from it. The coupled hinge is then placed in parallel with another coupled hinge creating a four bar linkage. With such a system, the rotations of one hinge are offset by another, and the connected bodies remain parallel while being displaced relative to one another. A sketch of the four bar linkage is shown in figure 4.3.

The mirror (reaction) axis features two four bar linkages alongside one another to constrain motion into a single dimension. A constructed mirror axis flexure is shown in figure 4.4. The vertical distance of each coupled hinge determines how much the mirror (counterweight) is displaced for a given hinge rotation, and thus the spring constant of the entire flexure system. The horizontal spacing between coupled hinges reduces compliance along non-desirable axes. The complete flexure system allows for the linear translation of the mirror (counterweight) without tilt, thus maintaining the desired parallelism.

#### 4.1.1 Predicted Compliance

Using Euler-Bernoulli beam theory, we can predict the compliance of the MTM flexure system, using Nicolae Lobontiu’s *Compliant Mechanisms: Design of Flexure Hinges* as a reference [23].



Figure 4.4: A constructed mirror axis flexure. A second one of these, behind, makes up the mirror axis.

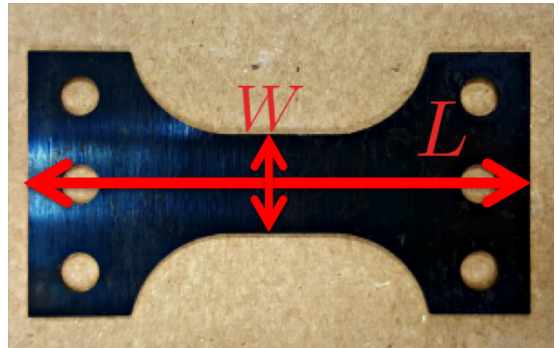


Figure 4.5: A sample flexure strap is shown with its width  $W$  and length  $L$  defined. The strap's thickness  $T$  is into the page.

First, we consider deflections along the flexure's preferred rotation axis, which we denote  $\hat{x}$ , when a force  $F$  is applied to the mirror (counterweight). First, we note that a deflection of the mirror (counterweight) along  $\hat{x}$  causes the flexure system to rotate at some angle  $\theta$ . The region that is rotated is the region between the two crosspoints of the individual flexure straps. Denote the length of this region  $H$ . For some deflection of the mirror (counterweight)  $\Delta x$ , we can see that  $\Delta x = H \sin \theta$ .

Now we consider an individual flexure strap. We model this as a cantilever beam having a rectangular cross section of constant area. We assume its elastic modulus,  $E$  and area moment of inertia,  $I$  do not change when the strap is bent. Under the Euler-Bernoulli theory of beams, the displacement  $w$  of a beam is related to its bending moment  $M$  as

$$\frac{d^2w}{dx^2} = -\frac{M(x)}{EI} \quad (4.1.1)$$

where we have introduced the coordinate  $x$  to represent length along the beam. This is distinct from the displacement of the flexure system  $\Delta x$ . For our flexure straps we write the bending moment as

$$M(x) = -\frac{F}{\sqrt{2}}(L - x)$$

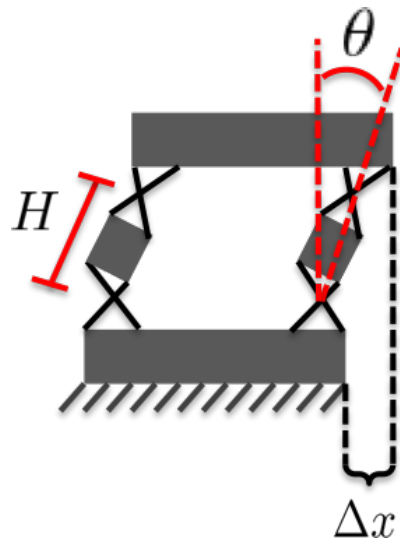


Figure 4.6: Relevant coordinates for our calculation of flexure system spring constant. For a displacement of the mirror or counterweight  $\Delta x$ , the mid section of each flexure hinge from flexure strap crosspoint to crosspoint, rotates an angle  $\theta$  relative to the endpoints. The crosspoint-crosspoint distance is denoted  $H$

Where we have introduced a factor of  $1/\sqrt{2}$  to account for the flexure strap being oriented  $45^\circ$  to the applied force.  $L$  is the length of a flexure strap. We can solve these equations to find the maximum displacement of the strap, which will occur at  $x = L$ , the ‘free’ end of the strap. The particular constants of integration are informed by boundary constraints. The maximum displacement is

$$w_{max} = \frac{L^3 F}{3\sqrt{2}EI} \quad (4.1.2)$$

giving an angular deflection

$$\sin \theta = \frac{L^2 F}{3\sqrt{2}EI} = \frac{4L^2 F}{\sqrt{2}EWT^3} \quad (4.1.3)$$

Where  $W$  is the width of a strap and  $T$  is its thickness, and we have used the relation  $I = WT^3/12$  for the beam’s moment of area about its center axis perpendicular to the force. Thus, we can solve for  $F/\Delta x$  and find the spring constant for a flexure strap is:

$$k_x = \frac{\sqrt{2}EWT^3}{4L^2H} \quad (4.1.4)$$

We treat each hinge as two springs in parallel, and each coupled hinge as two hinges in series. We assume all flexure straps have the same spring constant and see that a coupled hinge has the same

spring constant as given in equation 4.1.4. The mirror (reaction) axis features four coupled hinges in parallel, and so we find it has a spring constant

$$k_{MTM,x} = \frac{\sqrt{2}EWT^3}{L^2H} \quad (4.1.5)$$

We have approximated all flexures as identical, and use the one shown in figure 4.5 to define the length, width and thickness. We measure  $H = 4.33$  in (11 cm),  $L = 2.5$  in (6.35 cm),  $W = 0.5$  in (1.27 cm), and  $T = 0.039$  in (1.0 mm), and look up a standard elastic modulus of steel as  $200 \times 10^9$  N m<sup>-2</sup>. For these values we predict

$$k_{MTM,x} = 8.1 \text{ N mm}^{-1} \quad (4.1.6)$$

Of course, this calculation makes a significant number of simplifying assumptions. It should, however, give us an approximation to the spring constant of the flexure system. For a more precise number, we elect to measure the spring constant rather than improve the calculation.

### 4.1.2 Measurement of Compliance

An experiment has been performed to measure the spring constant of the flexure systems constructed for one of the W band VPMs. The complete flexure system was assembled, and secured to the VPM baseplate. The baseplate was clamped onto a breadboard securing it in place.

A force gauge was aligned to the center of the top part of the mirror (reaction) axis, and was secured to the translating portion of a micrometer stage. The micrometer stage was then secured to the breadboard. By translating the micrometer stage a set distance  $x$ , the force gauge was driven into the flexure system displacing it by  $x$ . The force exerted by the flexure system as it attempted to return to equilibrium could then be read out by the force gauge. The relationship between this force and the displacement is interpreted as the spring constant of the flexure system.

The force gauge used for this measurement was a Dillon<sup>3</sup> GL force gauge with a capacity of 25

---

<sup>3</sup>Dillon, 6429 Abrams Montreal (St-Laurent), QC H4S 1X9 Canada, <http://www.dillon-force.com/>

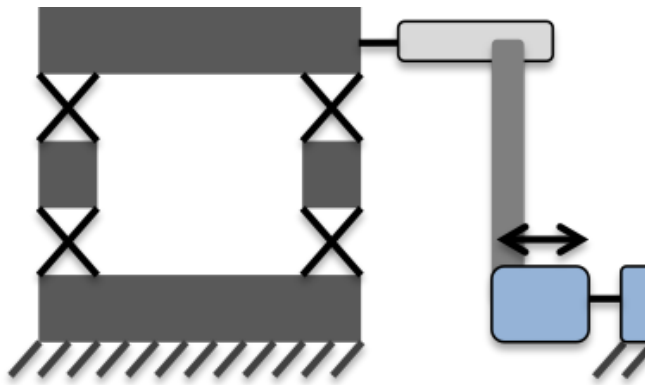


Figure 4.7: The experimental set up. The flexure system (left) was displaced from equilibrium by a force gauge (light grey) secured to a micrometer stage (light blue). By translating the stage, the flexure system was displaced a known distance, and its restoring force was measured with the force gauge.

N and a precision of  $\pm 0.1$  N. The micrometer stage was an Edmund Optics<sup>4</sup> linear translation stage with position markings at the 0.001 in (0.0025 cm) level.

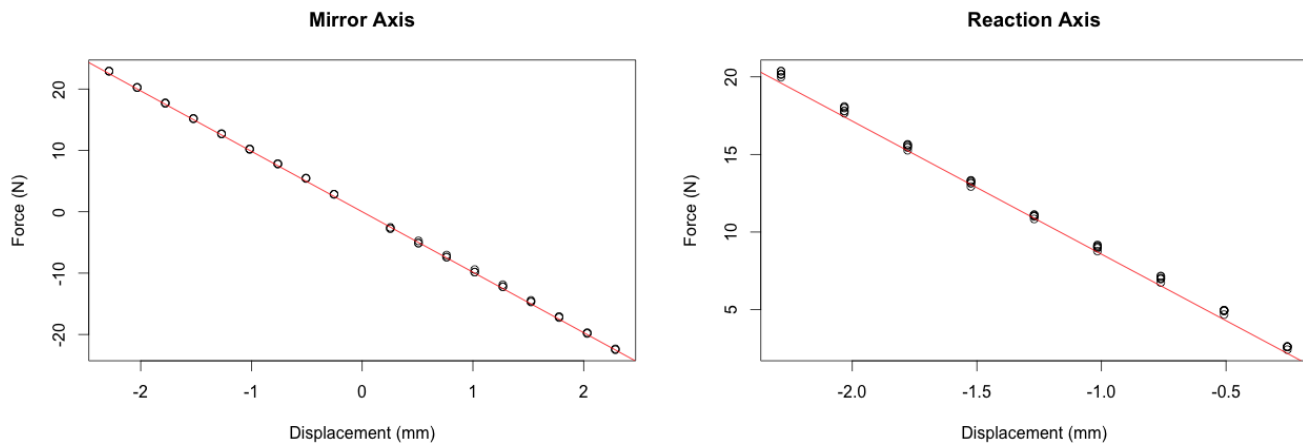
It was recognized that alignment of the force gauge with the flexure system such that the gauge is exactly in contact with the system when at equilibrium would be difficult. Thus, measurements were taken by first displacing the flexure a small amount and recording a set-point force and distance. All subsequent measurements for a single trial were recorded relative to this set-point. Between trials, the set-point was reset. As the relationship between force and distance is expected to be constant, this amounts to a vertical offset of the data relative to displacement from equilibrium values. It should not affect the measured spring constant.

Table 4.1: Measured spring constant values for the complete flexure system

MTM axis	Spring Constant (N/mm)	Error (N/mm)	$R^2$ value
Reaction	8.57	$\pm 0.043$	0.9987
Mirror	9.85	$\pm 0.017$	0.9998

For each trial, the displacement from the set-point was increased in increments of 0.01 in (0.254 cm) and the force was recorded from the gauge. The number of measurements in each trial was limited by the maximum force reading of the gauge, (25 N). This equated to 10 measurements. The set-point displacement and force for each trial was subtracted from subsequent measurements, and the set-point was discarded, giving 9 data points per trial. For the mirror axis, the displacement

<sup>4</sup>Edmund Optics, 101 East Gloucester Pike, Barrington, NJ 08007-1380 USA, <http://www.edmundoptics.com/>



was applied from both directions for 3 trials each. This amounted to a total of 54 data points. For the reaction axis, spatial constraints only permitted displacements to be applied from one direction, and 6 trials were performed for a total of 54 data points. The data for each axis was pooled and a linear regression on the data was performed in R. The data are plotted in figure 4.8 and the spring constant results are shown in table 4.1.

We can immediately see that the numbers are fairly close to the predicted spring constant. It is also comforting to see such a high value of  $R^2$ , indicating our data is very nearly linear. When we examine the residual plot, however, we can see that there appears to be a pattern, particularly on the reaction axis. This indicates that a linear fit may not be the best. Since we know the restoring force of a spring is linear with displacement, this tells us that there is likely unaccounted for error in our measurements.

The most likely source of this error was in the connection between the force gauge and the flexure system. The two were not secured to one another, but rather, were pressed tightly together. Because they were not secured, the two could have slipped relative to one another altering the angle between them. Such a change would cause the force read out to be not exactly the restoring force of the spring.

In the complete MTM assembly, additional elements will be attached to the flexure system, likely altering their spring constants. As such, when the MTM is fully assembled, a further measurement of the spring constant will be necessary.

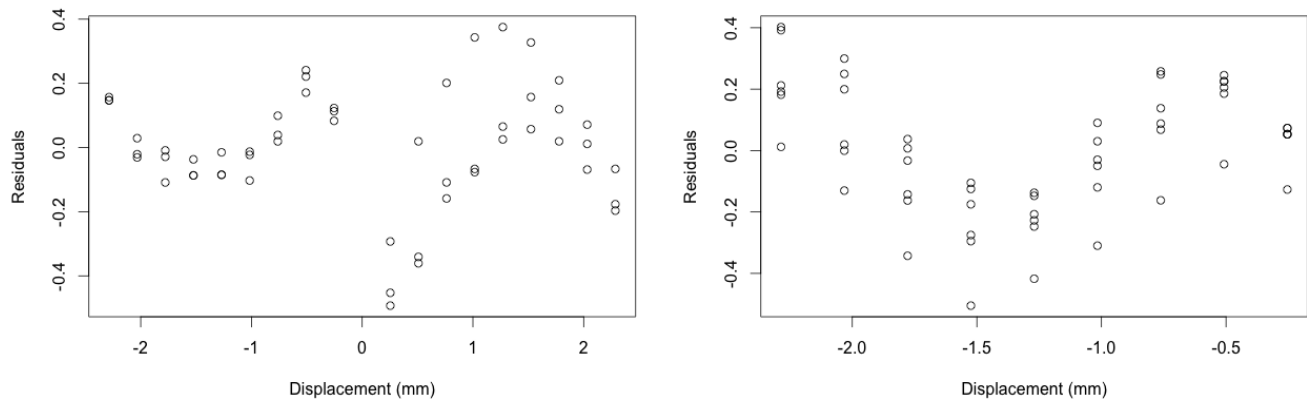


Figure 4.8: **Top:** Mirror (left) and Reaction (right) axis plots of force vs displacement and best fit line. **Bottom:** Residual plots for the best fit lines.

## 4.2 Electronic Components

### 4.2.1 Voice Coils

The devices used to provide force on the flexure system and thus drive the mirror are BEI Kimco linear voice coil actuators<sup>56</sup>. They provide a peak force of 60 lbs (266.9 N) and are cylindrically shaped 2.5 in (6.35 cm) in diameter and 4.17 in (10.59 cm) long. They provide a total stroke of 1 in (2.54 cm), and infinitely precise position sensitivity for a given current.

A voice coil is a coil of wire attached to the cone of a speaker. When current is driven through the coil a magnetic field is produced, which reacts with a magnet fixed to the frame of the speaker. The magnetic interaction moves the cone of the speaker. In this way, a voice coil transforms current into a force along the axis of the coil.

### 4.2.2 Linear Encoders

Position data of the mirror and counterweight are read out with ACU-RITE SENC 50 precision glass scale linear encoders<sup>7</sup>. These have a position resolution of 0.5  $\mu\text{m}$ , and are accurate to  $\pm 3 \mu\text{m}$ , while weighing 0.5 kg.

<sup>5</sup>BEI Kimoco, 1499 Poinsettia Avenue, Suite 160, Vista, CA 92081 USA, <http://www.beikimco.com/>

<sup>6</sup>Model number LA25-42-000A

<sup>7</sup>ACU-RITE, 333 State Parkway Schaumburg, IL 60173-5337, USA, <http://www.acu-rite.com/>

The encoders are connected such that one end is fixed to the MTM baseplate, and another is secured to the mirror or counterweight. They are optical encoders which detect position by illuminating an optical detector through a glass scale. The scale is coated with chrome in a regular pattern such that the signal on the detector is sinusoidal with position. A second scale and detector have a pattern  $90^\circ$  out of phase with the first, and is held stationary while the first is translated. By comparing the relative phase of the two and comparing to a reference mark, the encoder is able to accurately measure position.

The MTM also features encoders to measure the tilt and rotation of the mirror. These quantities are not used in the control system, but are exported to a mount computer for later analysis.

### 4.2.3 Vibration Sensor

A Measurement Specialties<sup>8</sup> MiniSense 100 vibration sensor is attached to the MTM baseplate. This device is a cantilever-beam loaded with a mass that creates a piezoelectric response under strain. When the sensor is accelerated normal to its beam, it produces a voltage response of 1.1 V/g (6 V/g at a resonance frequency of 75 Hz).

## 4.3 Control Systems

The MTM features a closed loop control system in order to ensure the mirror moves as desired, and to ensure minimal vibrations of the telescope. The positions of the mirror and counterweight are continuously read in via glass slide encoders, and used to inform the current output of the voice coils. Additional encoders read the tilt and rotation of the mirror. There is a vibration sensor attached to the baseplate of the MTM which measures the vibrations of the telescope.

### 4.3.1 Model

To begin to determine how to control this system, we first model the MTM as a linear damped, driven spring system like shown in figure 4.9. We define our coordinates so that  $+x$  points to the left on the image. The 0 subscript refers to quantities on the mirror axis, and the 1 subscript to

---

<sup>8</sup>Measurement Specialties 1000 Lucas Way Hampton, VA 23666, USA, <http://www.meas-spec.com>

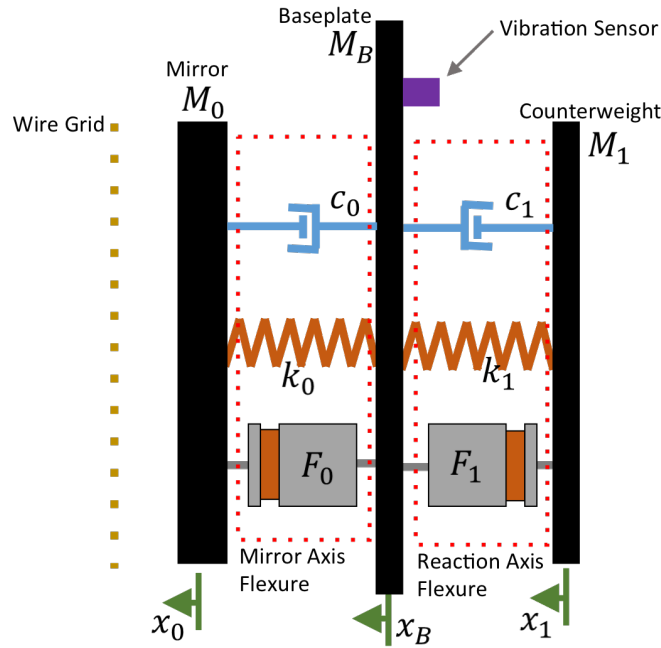


Figure 4.9: The damped driven spring system model of the MTM.  $x_0$  and  $x_1$  relative to  $x_B$  are read by linear encoders, and  $F_0$  and  $F_1$  are controlled by the current fed to the voice coils.

those on the reaction axis. The  $B$  axis denotes quantities of the system's baseplate, which is secured to the telescope mount. From such a system, we can write the force balance equations as:

$$M_0 \ddot{x}_0 = F_0 - c_0(\dot{x}_0 - \dot{x}_B) - k_0(x_0 - x_B) \quad (4.3.1)$$

$$M_B \ddot{x}_B = -F_0 + F_1 + c_0(\dot{x}_0 - \dot{x}_B) - c_1(\dot{x}_B - \dot{x}_1) + k_0(x_0 - x_B) - k_1(x_B - x_1) \quad (4.3.2)$$

$$M_1 \ddot{x}_1 = -F_1 + c_1(\dot{x}_B - \dot{x}_1) + k_1(x_B - x_1) \quad (4.3.3)$$

In principle, we can solve these equations exactly and determine the form of  $F_0(t)$  and  $F_1(t)$  that give the desired position functions. In reality, the VPM system isn't perfectly linear as just modeled. Outside sources such as wind disturb the system in unpredictable ways, and the motion of the mount introduces Coriolis and centrifugal forces. We require a degree of accuracy that the linear model does not provide. To account for this, we use a control system.

We translate these into state space equations by defining  $\vec{x} = (x_0, \dot{x}_0, x_1, \dot{x}_1, x_B, \dot{x}_B)^T$  as the state of the system, and the system input as  $\vec{u} = (F_0, F_1)^T$  [2]. Our state space equation is  $\dot{\vec{x}} = A\vec{x} + B\vec{u}$  for

$$A = \begin{pmatrix} 0 & 1 & 0 & 0 & 0 & 0 \\ -k_0/M_0 & -c_0/M_0 & 0 & 0 & k_0/M_0 & c_0/M_0 \\ 0 & 0 & 0 & 1 & 0 & 0 \\ 0 & 0 & -k_1/M_1 & -c_1/M_1 & k_1/M_1 & c_1/M_1 \\ 0 & 0 & 0 & 0 & 0 & 1 \\ k_0/M_B & c_0/M_B & k_1/M_B & c_1/M_B & -(k_0 + k_1)/M_B & -(c_0 + c_1)/M_1 \end{pmatrix} \quad (4.3.4)$$

$$B = \begin{pmatrix} 0 & 1 & 0 & 0 & 0 & -1 \\ 0 & 0 & 0 & -1 & 0 & 1 \end{pmatrix}^T \quad (4.3.5)$$

We model the output of our system as  $\vec{y} = C\vec{x}$  for

$$C = \begin{pmatrix} 1 & 0 & 0 & 0 & -1 & 0 \\ 0 & 0 & 0 & 0 & 0 & 0 \\ 0 & 0 & 1 & 0 & -1 & 0 \\ 0 & 0 & 0 & 0 & 0 & 0 \\ 0 & 0 & 0 & 0 & 0 & 0 \\ 0 & 0 & 0 & 0 & 0 & 0 \end{pmatrix} \quad (4.3.6)$$

Which corresponds to measuring the relative displacements  $x_0 - x_B$  and  $x_1 - x_B$ . For a system like the VPM, the outputs have desired values as a function of time, denoted  $\vec{x}^*$ . For the VPM, this corresponds to the desired mirror drive function and counterweight position. To control the system, we define the error  $\vec{e}$  as  $\vec{y} - \vec{x}^*$  and modify the inputs based on the error. For a simple proportional controller, this takes the form

$$\vec{u}_2 = P\vec{e}_1 \quad (4.3.7)$$

Where we have used the subscripts 2 and 1 to denote that the error is used to update subsequent inputs. The matrix  $P$  has values chosen experimentally to limit  $\vec{e} \rightarrow 0$  as  $t \rightarrow \infty$ .

### 4.3.2 CLASS control systems

The specific control system for class is slightly different from that described above. The position data read out includes both the DC position and amplitude of AC oscillations for both bodies, as well as the relative phase between the two. The input vector has corresponding DC current and amplitude of AC current, and a phase difference between  $I_0$  and  $I_1$ . Note that we have switched from the force,  $F$ , to the current,  $I$ . This does not significantly change our discussion as the voice coils put the two in a 1–1 correspondence.

We write the position vector  $\vec{x}$  as  $(x_{amp,0}, x_{dc,0}, x_{amp,1}, x_{dc,1}, \phi_{01})^T$ , and the input vector as  $\vec{u} = (I_{amp,0}, I_{dc,0}, I_{amp,1}, I_{dc,1}, \varphi_{01})^T$ . We can then measure the system matrix  $A$  by recording changes in  $\vec{x}$  for changes in individual components of  $\vec{u}$ . For the W band VPM which was constructed, this measurement of  $A$  postdates this document. With the system matrix known, we can implement a control system and achieve the desired functionality. The control system is run on an ACS SPiiPlus motion controller<sup>9</sup> which outputs commands to an ACS UDMnt driver, which controls the voice coil current. A sketch of the MTM control system is shown in figure 4.10

---

<sup>9</sup>ACS Motion Control, 7444 W 78th Street Bloomington, MN 55439, USA, <http://www.acsmotioncontrol.com/>

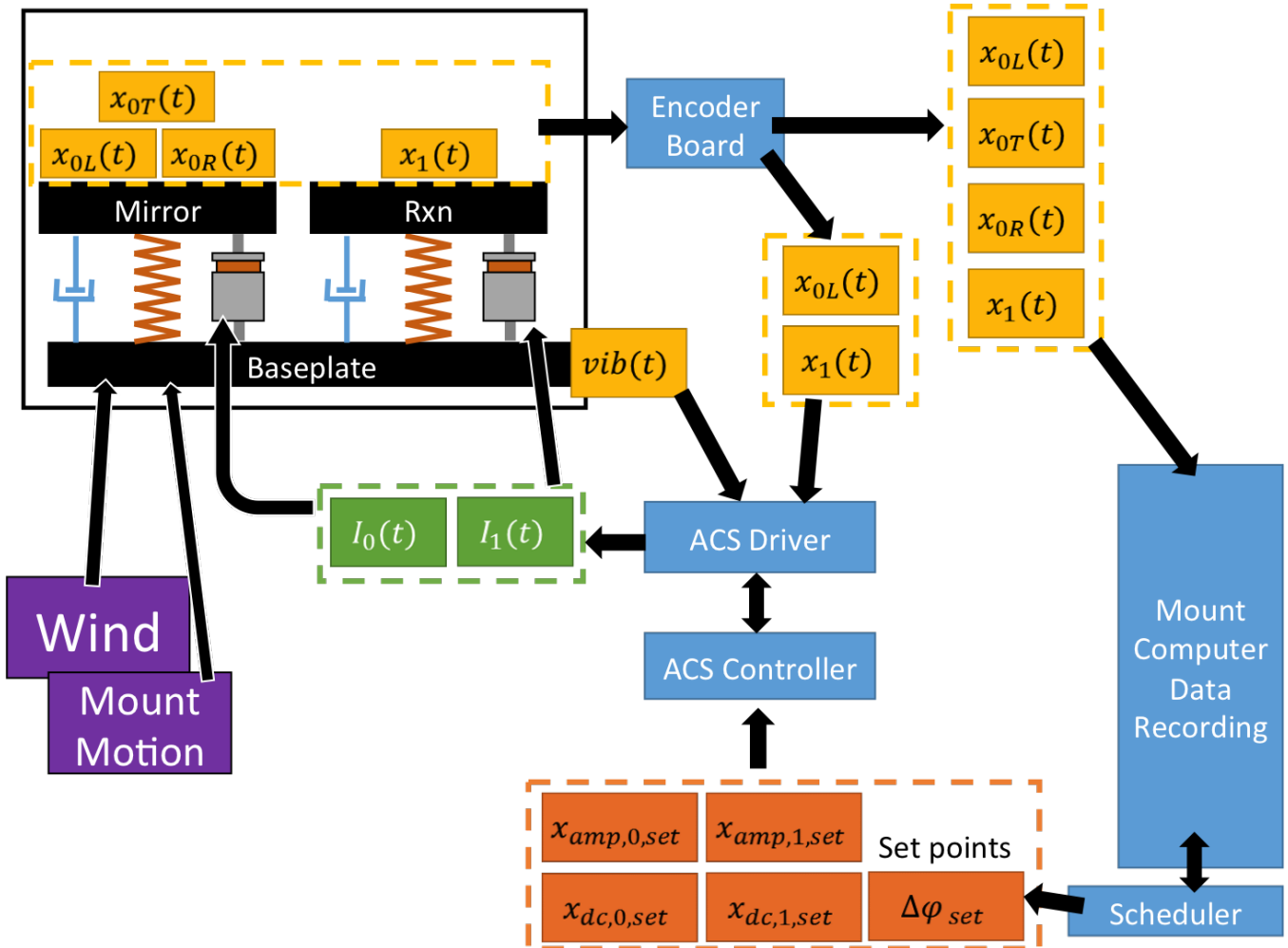


Figure 4.10: The MTM control system. A mount computer sets the desired position for the mirror and counterweight to allow for proper VPM functionality and minimal base vibrations, as well as the phase difference between the two. This information is fed through the ACS controller and into the ACS driver, which sets the voice coil currents. Voice coils and external sources (purple boxes) move the MTM system, and mirror and counterweight positions are read out by a series of linear encoders. The positions are recorded by the mount computer, and fed back into the ACS driver. A vibration sensor on the baseplate also informs the ACS driver, which then updates the current directed to the voice coils in response to the current position.

# Chapter 5

## Summary

In this document we have presented the necessary cosmological background to understand the theory of inflation and evidence for its detection in the form of  $B$  mode polarization of the CMB. We have discussed CLASS, a leading experiment in making measurements of these  $B$  modes, with emphasis on the CLASS polarization modulators, VPMs. A W band VPM was modeled and we conclude that it must be driven at an amplitude of  $\sim 1$  mm to function as desired. We discussed the VPM mirror transport mechanisms, in particular their flexure systems. We have predicted the flexure systems to have a spring constant of  $k_{MTM} = 8.1 \text{ N mm}^{-1}$  and measured the mirror and reaction axes to have spring constants of  $k_{mirror} = 9.85 \pm 0.017 \text{ N mm}^{-1}$  and  $k_{reaction} = 8.57 \pm 0.043 \text{ N mm}^{-1}$ .

# Appendices

# Appendix A

## Optical Background

In this section we will discuss the background optics used throughout the rest of the document. We begin by discussing the standard interpretation of polarized light, before discussing Stokes parameters and the Jones matrix formalism. The latter two are particularly important for our analysis of the CLASS VPM.

### A.1 Polarized light

All light carries with it an electric and magnetic field, which are both orthogonal to each other, and the direction of propagation of the light. If the electric field has a particular orientation, the light is said to be polarized, whereas if it is random in nature, the light is unpolarized. Light from most natural sources consists of waves with an arbitrary, varying succession of different electric fields and is unpolarized. In general, most light is some combination of polarized and unpolarized light [14]. A particular polarization orientation for beams of light is referred to as a polarization state.

Consider a monochromatic beam of light propagating in the  $\hat{z}$  direction. A fully polarized such beam can be described by its electric field as

$$\vec{E} = E_x \cos(kz - \omega t) \hat{x} + E_y \cos(kz - \omega t - \delta) \hat{y} \quad (\text{A.1.1})$$

where  $k$  is the wavenumber,  $\omega$  is the frequency, and  $\delta$  is the relative phase difference between  $\hat{x}$  and  $\hat{y}$  components. The  $\hat{x}$  and  $\hat{y}$  components add vectorially to produce the observed electric field.

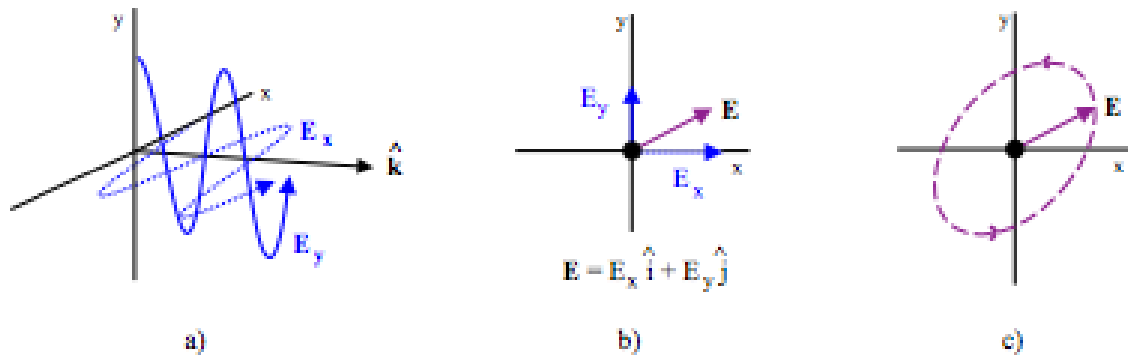


Figure A.1: a)  $\hat{x}$  and  $\hat{y}$  components of electric field of a polarized wave. b) Vector sum of those components for all times for fixed  $z$ . c) The locus of points that will be traced out by that sum. This wave is elliptically polarized. Image from Jo-Anne Brown, [5]

When  $\delta = 0, \pi$ , the vector sum is constrained along a single line, and the polarization is called linear. When  $\delta = \pm\frac{\pi}{2}$ ,  $E_x = E_y$ , the vector sum traces out a circle, and the polarization is circular. Any other case is called elliptical polarization.

We can see that the polarization vector for fixed  $z$  traces out an ellipse on the  $\hat{x} - \hat{y}$  plane as follows. Take  $z = 0$ , and define:

$$\vec{E}_x = E_x \cos(\omega t) \quad (\text{A.1.2})$$

$$\vec{E}_y = E_y \cos(\omega t + \delta) = E_y [\cos(\omega t) \cos(\delta) - \sin(\omega t) \sin(\delta)] \quad (\text{A.1.3})$$

Motivated by observing the polarization traces an ellipse over time, we cancel the  $\omega t$  dependance by plugging A.1.2 into A.1.3 and simplifying to get:

$$\frac{\vec{E}_y}{E_y} = \cos(\delta) \frac{\vec{E}_x}{E_x} - \sin(\delta) \sqrt{1 - \left( \frac{\vec{E}_x}{E_x} \right)^2} \quad (\text{A.1.4})$$

$$\sin^2(\delta) = \left( \frac{\vec{E}_y}{E_y} \right)^2 + \left( \frac{\vec{E}_x}{E_x} \right)^2 - 2 \frac{\vec{E}_y}{E_y} \frac{\vec{E}_x}{E_x} \cos(\delta) \quad (\text{A.1.5})$$

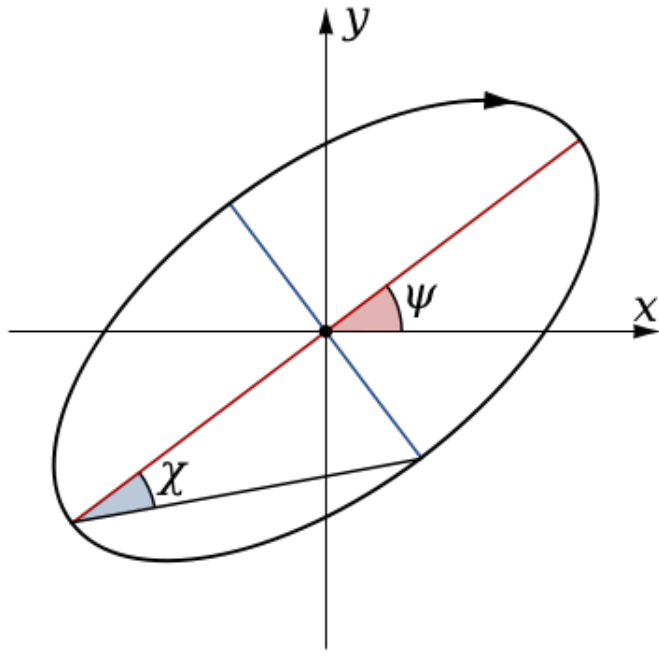


Figure A.2: Partial parameterization of the polarization ellipse.  $\psi$  indicates the tilt, or the deviation of the major axis from the  $\hat{x}$  axis.  $\chi$  denotes the ellipticity angle. To fully characterize this ellipse we require the length of the major or minor axis, or the intensity [19].

or,

$$1 = a\vec{E}_x^2 + b\vec{E}_y^2 + c\vec{E}_x\vec{E}_y \quad (\text{A.1.6})$$

$$a = \frac{1}{\sin^2 \delta E_x^2}, \quad b = \frac{1}{\sin^2 \delta E_y^2}, \quad c = \frac{-2 \cos \delta}{E_x E_y \sin^2 \delta} \quad (\text{A.1.7})$$

This represents a general ellipse. To describe this ellipse we require three parameters: a tilt angle  $\psi$ , an ellipticity angle  $\chi$ , and the intensity of the polarized light. To find these, we first perform a coordinate rotation by an angle  $\psi$ :  $\hat{x} \rightarrow \hat{x} \cos(\psi) - \hat{y} \sin(\psi)$ ,  $\hat{y} \rightarrow \hat{x} \sin(\psi) + \hat{y} \cos(\psi)$ . Applied to our polarization ellipse this gives

$$1 = a'\vec{E}_x^2 + b'\vec{E}_y^2 + c'\vec{E}_x\vec{E}_y \quad (\text{A.1.8})$$

$$a' = a \cos^2(\psi) + b \sin^2(\psi) + c \cos(\psi) \sin(\psi) \quad (\text{A.1.9})$$

$$b' = a \sin^2(\psi) + b \cos^2(\psi) - c \cos(\psi) \sin(\psi) \quad (\text{A.1.10})$$

$$c' = -2a \cos(\psi) \sin(\psi) + 2b \cos(\psi) \sin(\psi) + c [\cos^2(\psi) - \sin^2(\psi)] \quad (\text{A.1.11})$$

To put our equation in canonical form, we wish to cancel the  $\vec{E}_x \vec{E}_y$  component, equivalent to  $c' = 0$ , or

$$\frac{c}{a - b} = \tan(2\psi) \quad (\text{A.1.12})$$

Plugging in values of  $a, b, c$ , this gives

$$\psi = \frac{1}{2} \arctan \left( \frac{-2 \cos(\delta)}{E_y^2 - E_x^2} \right) \quad (\text{A.1.13})$$

From this the following relations to deduce the other necessary parameters

$$A = \sqrt{\frac{1}{a'}} \quad (\text{A.1.14})$$

$$B = \sqrt{\frac{1}{b'}} \quad (\text{A.1.15})$$

$$\chi = \arctan\left(\frac{B}{A}\right) \quad (\text{A.1.16})$$

The length of the major or minor axes,  $A$  and  $B$  can be used in place of the intensity to describe the polarization state.

## A.2 Stokes Parameters

An alternative parameterization of the polarization ellipse was given by Stokes in 1852. These are Stokes parameters and are given here without derivation [5].

$$I = \langle E_x \rangle^2 + \langle E_y \rangle^2 \quad (\text{A.2.1})$$

$$Q = \langle E_x \rangle^2 - \langle E_y \rangle^2 = I_p \cos(2\chi) \cos(2\psi) \quad (\text{A.2.2})$$

$$U = 2 \langle E_x E_y \cos(\delta) \rangle = I_p \cos(2\chi) \sin(2\psi) \quad (\text{A.2.3})$$

$$V = 2 \langle E_x E_y \sin(\delta) \rangle = I_p \sin(2\chi) \quad (\text{A.2.4})$$

$I$  describes the intensity of the light,  $I_p$  the intensity of the polarized light, and  $Q, U, V$  define components of the polarization. We have also dropped our assumption of monochromatic light,

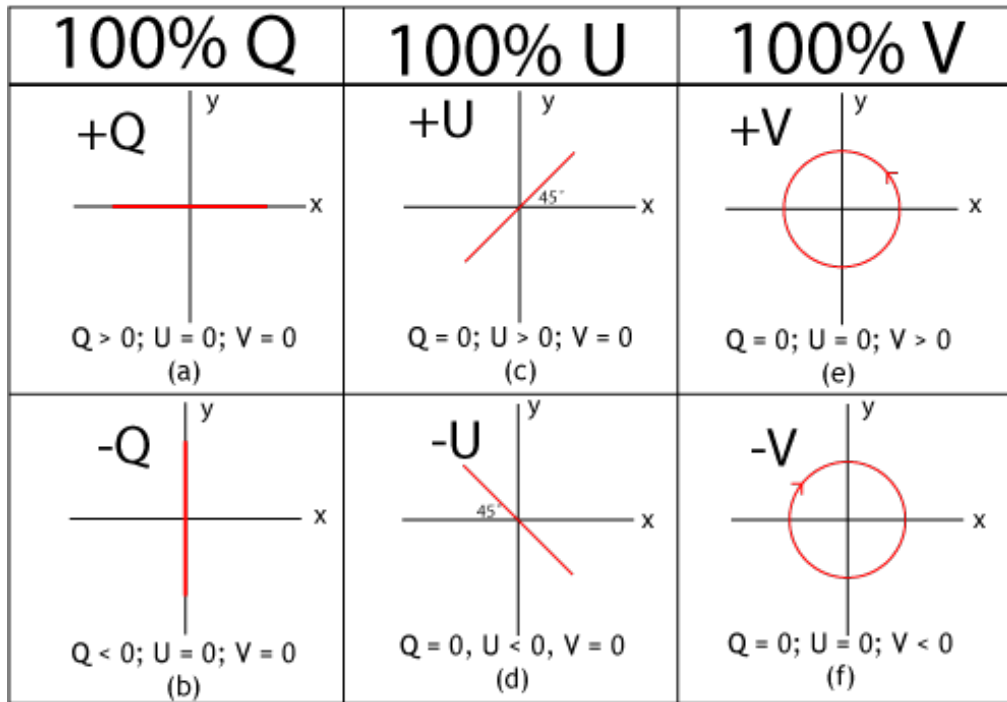


Figure A.3: Stokes parameters.  $Q$  represents linear polarization along the axes, and  $U$  represents linear polarization  $45^\circ$  to the axes.  $V$  represents circular polarization. These form a basis that fully parameterizes the polarization ellipse and can describe a general polarization [28].

requiring the inclusion of the time averaged electric fields. Light that is fully polarized will obey the relation  $I = I_p$ . Partially polarized light obeys  $I \geq I_p$ . We define the polarization fraction,  $P$  as  $P = I_p/I$ , which describes the degree to which light is polarized.

These parameters are convenient because they neatly describe special polarization states. Unpolarized light will have  $Q, U, V = 0$ . Linearly polarized light along the axes can be described solely in terms of  $Q$ , with  $+Q$  describing horizontal polarization, and  $-Q$  describing vertical. Linearly polarized light  $45^\circ$  to the axes can be described solely in terms of  $U$ , with  $+U$  describing light  $+45^\circ$  to the x-axis and  $-U$  being  $-45^\circ$  to the x-axis. Circularly polarized light can be described solely with  $V$  with  $+V$  describing right-hand circular polarization and  $-V$  left. These are summarized in figure A.3.

The Stokes parameters are analogous to spherical coordinates with  $I_p$ ,  $2\psi$ , and  $2\chi$  taking the place of  $r, \theta, \phi$ . When considered this way, a polarization state can be viewed as a point on a sphere. This sphere is known as the Poincaré sphere.

### A.2.1 Rotations

In this section we consider how Stokes parameters transform under rotations. Suppose we have polarized light propagating in the  $\hat{z}$  direction described by the four Stokes parameters. First we consider a rotation based on the alternate parameterization,  $I, \chi, \psi$ . It is easy to see that under a rotation of the axes by an angle  $\theta$ , these become  $I, \chi, (\psi - \theta)$ . Observing equations A.2.1-A.2.4, we see the Stokes parameters transform as:

$$I \rightarrow I \quad (\text{A.2.5})$$

$$Q \rightarrow Q \cos(2\theta) + U \sin(2\theta) \quad (\text{A.2.6})$$

$$U \rightarrow U \cos(2\theta) - Q \sin(2\theta) \quad (\text{A.2.7})$$

$$V \rightarrow V \quad (\text{A.2.8})$$

For the Stokes parameters describing linear polarization  $(Q, U)$ , this is equivalent to

$$\begin{pmatrix} Q \\ U \end{pmatrix} \rightarrow \begin{pmatrix} \cos 2\theta & \sin 2\theta \\ -\sin 2\theta & \cos 2\theta \end{pmatrix} \begin{pmatrix} Q \\ U \end{pmatrix} \quad (\text{A.2.9})$$

Or in terms of a standard rotation matrix, we can see

$$\begin{pmatrix} Q & U \\ U & -Q \end{pmatrix} \rightarrow \begin{pmatrix} \cos \theta & \sin \theta \\ -\sin \theta & \cos \theta \end{pmatrix} \begin{pmatrix} Q & U \\ U & -Q \end{pmatrix} \begin{pmatrix} \cos \theta & -\sin \theta \\ \sin \theta & \cos \theta \end{pmatrix} \quad (\text{A.2.10})$$

This is equivalent to how a  $2 \times 2$  tensor changes under rotation, and so the linear Stokes parameters  $(Q, U)$  can be described by the symmetric, traceless  $2 \times 2$  tensor above. This allows them to be described as a spin-2 field. [6].

### A.2.2 Stokes Vectors

Stokes parameters can be compactly written as a vector with four components. When doing so it is convention to normalize the parameters by dividing each by  $I$ . Thus any general polarization state

$\mathcal{P}$  can be written as

$$\mathcal{P} = \begin{pmatrix} 1 \\ Q/I \\ U/I \\ V/I \end{pmatrix}$$

As an example, for unpolarized light we have  $\mathcal{P} = (1, 0, 0, 0)^T$  and for fully vertical polarized light we have  $\mathcal{P} = (1, -1, 0, 0)^T$ .

### A.3 Jones Matrices

Another representation of polarized light which will be of use for describing the optical elements of the CLASS telescope is known as Jones vectors and Jones matrices, invented by R. Clark Jones in 1941 [14]. This formalism describes only fully polarized light. If we consider the light wave given in equation A.1.1, the Jones vector is given as

$$\vec{E} = \begin{pmatrix} E_x \\ E_y \end{pmatrix} \quad (\text{A.3.1})$$

Again, it is convention to normalize the Jones vector to have magnitude unity. The Jones vectors for special polarization states are given in Table A.1.

The Jones vector formalism is convenient in that orthogonal polarization states will be represented by orthogonal Jones vectors. Additionally, optical elements which transform polarization states will be represented mathematically by a  $2 \times 2$  Jones matrix denoted  $J$ . If light is passed through multiple optical elements, each of which changes the polarization state with  $J_1$  being the first element,  $J_2$  the second and so on, we can write

$$\vec{E}_f = J_n \dots J_2 J_1 \vec{E}_1 \quad (\text{A.3.2})$$

Table A.1: Jones vectors for various polarization states

Polarization state	Stokes Parameter	Jones Matrix
Horizontal	$+Q$	$\begin{pmatrix} 1 \\ 0 \end{pmatrix}$
Vertical	$-Q$	$\begin{pmatrix} 0 \\ 1 \end{pmatrix}$
$+45^\circ$	$+U$	$\frac{1}{\sqrt{2}} \begin{pmatrix} 1 \\ 1 \end{pmatrix}$
$-45^\circ$	$-U$	$\frac{1}{\sqrt{2}} \begin{pmatrix} 1 \\ -1 \end{pmatrix}$
Right-hand circular	$+V$	$\frac{1}{\sqrt{2}} \begin{pmatrix} 1 \\ -i \end{pmatrix}$
Left-hand circular	$-V$	$\frac{1}{\sqrt{2}} \begin{pmatrix} 1 \\ i \end{pmatrix}$

# Appendix B

## Thomson Scattering

In this section we describe the Thomson scattering of an electromagnetic wave off of a free electron. Thomson scattering is the low-energy, non-relativistic limit of photon electron scattering, which is valid when  $h\nu \ll m_ec^2$ . For CMB photons this is an appropriate approximation. First we will treat the Thomson scattering of a polarized plane wave and then an unpolarized plane wave. Next we will consider the scattering of an unpolarized radiation field.

Consider an electromagnetic wave propagating in the  $\hat{x}$  direction, carrying linear polarization in the  $\hat{z}$  direction, with an observer along the  $\hat{y}$  axis.

$$\vec{E} = \hat{z}E_0 \cos(\vec{k} \cdot \vec{r} - \omega t) \quad (\text{B.1})$$

When this wave is incident on an electron at the origin, the electron experiences a force

$$\vec{F} = q\vec{E} = -eE_0 \cos(\omega t)\hat{z} \quad (\text{B.2})$$

Where we have neglected the magnetic field as it carries a prefactor  $\beta$  which is negligible in the non-relativistic regime we are considering. This force causes the electron to oscillate in the  $\hat{z}$  direction, and the system can be considered an electric dipole with dipole moment

$$\vec{p} = -\frac{e^2 E_0}{m\omega^2} \cos(\omega t)\hat{z} \quad (\text{B.3})$$

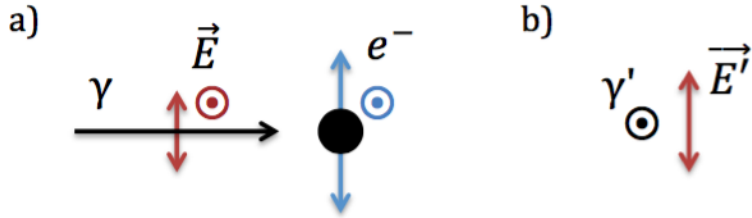


Figure B.1: Thomson Scattering of unpolarized polarized light off free electron. a) Light ( $\gamma$ ) with polarization components ( $\vec{E}$ ) into and vertical on the page given by the red arrows is incident on a free electron causing it to oscillate with components given by the blue arrows. b) An observer looking down on the page will see scattered light  $\gamma'$  with polarization ( $\vec{E}'$ ) given by the second red arrow. The scattered light is linearly polarized and parallel to one component of the incident light's polarization.

We assume that this is a perfect dipole, and it radiates energy with intensity and electric field [11]

$$\vec{I} = \frac{\mu_0}{32\pi^2 c} \left( \frac{e^2 E_0}{m} \right)^2 \frac{\sin^2 \theta}{r^2} \hat{r} \quad (\text{B.4})$$

$$\vec{E} = \frac{\mu_0}{4\pi c} \frac{e^2 E_0}{m} \left( \frac{\sin \theta}{r} \right) \cos[\omega(t - r/c)] \hat{\theta} \quad (\text{B.5})$$

Where  $r$  just represents distance of a point from the dipole, and  $\hat{r}$  the direction to that point and  $\theta$  the angle from the  $z$ -axis (the direction of incoming polarization). We will ignore magnitudes of these quantities and focus on their directions.

Due to the  $\sin^2 \theta$  term, intensity peaks in the  $\hat{x} - \hat{y}$  plane, perpendicular to the incident polarization, and intensity is 0 in the  $\hat{z}$  direction. The electric field, which defines the polarization of the scattered light, is in the  $\hat{\theta}$  direction, which means that for an observer along the  $\hat{y}$  axis, the scattered light is linearly polarized along the  $\hat{z}$  axis, parallel to the incident polarization. Similarly, for light incident from the  $\hat{z}$  axis with polarization in the  $\hat{x}$  direction, the scattered light remains polarized in the  $\hat{x}$  direction. Simply put, Thomson scattering produces radiation peaking in the plane of the incident light, with polarization parallel to the incident polarization.

We observe that if the incident wave had a polarization component in the  $\hat{y}$  direction, it causes the electron to oscillate in that direction and scatters no light to the observer. Thus, for any

polarization of the light incident from the  $\hat{x}$  direction (other than fully linearly polarized along  $\hat{y}$ , but including unpolarized light), the scattered light will be polarized linearly along  $\hat{z}$ . More precisely, we can write that for any incident polarization along  $\hat{\varepsilon}$  and scattered polarization along  $\hat{\varepsilon}'$  [6]

$$\frac{d\sigma}{d\Omega} = \frac{3\sigma_T}{8\pi} |\hat{\varepsilon} \cdot \hat{\varepsilon}'|^2 \quad (\text{B.6})$$

Where  $\sigma_T$  is the Thomson Scattering Cross section, a constant.

## B.1 Unpolarized Incident Light

Now, what if the incoming light is unpolarized? For this analysis, we follow Kosowsky's Introduction to Microwave Background Polarization [21]. Suppose we have an incident plane wave of unpolarized light with Intensity  $I'$ , cross-sectional area  $\sigma_B$  scattering from the  $\hat{x} - \hat{y}$  plane into the  $\hat{y}$  direction. We will describe the scattered light in terms of Stokes Parameters, described in section A.2. We define the Stokes parameters with respect to the z-axis (i.e.  $+Q$  is along the z-axis). We then see

$$I = \frac{3\sigma_T}{8\pi\sigma_B} I' (1 + \cos^2\theta) \quad (\text{B.1.1})$$

$$Q = \frac{3\sigma_T}{8\pi\sigma_B} I' \sin^2\theta \quad (\text{B.1.2})$$

$$U = 0 \quad (\text{B.1.3})$$

$$V = 0 \quad (\text{B.1.4})$$

Where  $\theta$  is the angle between incoming and outgoing radiation. So we can see that for incident, unpolarized light along the x-axis with an observer in the y-axis, the scattered light is linearly polarized in the  $\hat{z}$  direction, as previously mentioned. If we let the incident intensity vary by angle,  $I' \rightarrow I'(\theta, \phi)$  and integrate over all incoming directions, we will see the net polarization from the scattering of an unpolarized radiation field. To do so, we expand the incident radiation field in terms of spherical harmonics:

$$I'(\theta, \phi) = \sum_{lm} a_{lm} Y_{lm}(\theta, \phi) \quad (\text{B.1.5})$$

The result for the scattered intensity and polarization is:

$$I(\hat{z}) = \frac{3\sigma_T}{16\pi\sigma_B} \left( \frac{8}{3}\sqrt{\pi}a_{00} + \frac{4}{3}\sqrt{\frac{\pi}{5}}a_{20} \right) \quad (\text{B.1.6})$$

$$Q(\hat{z}) = \text{Re} \left[ \frac{3\sigma_T}{4\pi\sigma_B} \sqrt{\frac{2\pi}{15}}a_{22} \right] \quad (\text{B.1.7})$$

$$U(\hat{z}) = -\text{Im} \left[ \frac{3\sigma_T}{4\pi\sigma_B} \sqrt{\frac{2\pi}{15}}a_{22} \right] \quad (\text{B.1.8})$$

$$V(\hat{z}) = 0 \quad (\text{B.1.9})$$

This is the result for outgoing polarization along the z-axis. If we then rotate our coordinates to consider outgoing polarization along a general direction  $\hat{n}$ , we transform  $a_{22}$  into a function of  $a_{2m}$  for  $m \in [-2, 2]$ . Thus

$$Q(\hat{n}) = \text{Re} \left[ \frac{3\sigma_T}{4\pi\sigma_B} \sqrt{\frac{2\pi}{15}} \sum_{m=-2}^2 f_m(\hat{n})a_{2m} \right] \quad (\text{B.1.10})$$

$$U(\hat{n}) = -\text{Im} \left[ \frac{3\sigma_T}{4\pi\sigma_B} \sqrt{\frac{2\pi}{15}} \sum_{m=-2}^2 f_m(\hat{n})a_{2m} \right] \quad (\text{B.1.11})$$

$$V(\hat{n}) = 0 \quad (\text{B.1.12})$$

If the incident radiation field has a quadrupolar anisotropy, then some of the  $a_{2m}$  will be non-zero and the scattered radiation will be polarized.

Thus, we see that Thomson scattering of an unpolarized radiation field produces outgoing linear polarization when there is a quadrupolar anisotropy in the incident field.

## Appendix C

# Curvature of the Universe

Just as Einstein showed that space is curved locally by matter, space could be curved on scales of the observable universe, or larger. There are three categories for the curvature of space: it could be positively curved, negatively curved, or flat. An example of positive (or closed) curvature in 2 dimensions is the surface of a sphere. An example of a 2-d negatively curved (or open) surface is a hyperboloid, and a flat 2-d surface is a plane. In cosmology, the curvature of the universe is related to the energy density  $\varepsilon$  by the Friedmann equation.

$$H(t)^2 = \frac{8\pi G}{3c^2} \varepsilon(t) - \frac{\kappa c^2}{R_0^2 a(t)^2} \quad (\text{C.1})$$

Friedmann Equation

Here,  $H(t)$  is the Hubble parameter,  $G$  is Newton's gravitation constant,  $a$  is the scale factor,  $c$  is the speed of light and  $R_0$  is the radius of curvature of the universe at present time.  $\kappa$  is a constant describing the curvature of space, taking values  $\kappa = +1$  for positive curvature,  $\kappa = -1$  for negative curvature, and  $\kappa = 0$  for a flat universe. For some critical value of energy density,  $\varepsilon = \varepsilon_c$ , we will have

$$H(t)^2 = \frac{8\pi G}{3c^2} \varepsilon_c(t) \quad (\text{C.2})$$

and  $\kappa = 0$ . Thus for  $\varepsilon = \varepsilon_c$ , the universe is spatially flat. for  $\varepsilon > \varepsilon_c$  the universe is positively curved, and for  $\varepsilon < \varepsilon_c$  the universe is negatively curved. To simplify this, we introduce the density

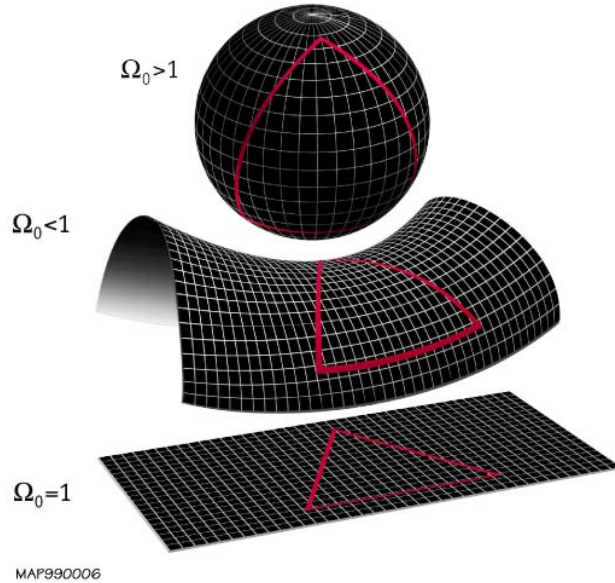


Figure C.1: Depictions of various spatial curvatures in 2 dimensions, with corresponding density parameters. A positively curved space is like the surface of a sphere and has density parameter  $\Omega_0 > 1$ . An example of a negatively curved space is the surface of a hyperboloid with  $\Omega_0 < 1$  and a flat space is like the surface of a plane with  $\Omega_0 = 1$  [29].

parameter  $\Omega$

$$\Omega(t) \equiv \frac{\varepsilon(t)}{\varepsilon_c(t)} \quad (\text{C.3})$$

And observe that for  $\Omega_0 > 1$  the universe is positively curved, for  $\Omega_0 < 1$  the universe is negatively curved, and for  $\Omega_0 = 1$  the universe is flat.

# References

- [1] P. A. R. Ade, N. Aghanim, Z. Ahmed, R. W. Aikin, K. D. Alexander, M. Arnaud, J. Aumont, C. Baccigalupi, A. J. Banday, D. Barkats, R. B. Barreiro, J. G. Bartlett, N. Bartolo, E. Battaner, K. Benabed, A. Benoît, A. Benoit-Lévy, S. J. Benton, J.-P. Bernard, M. Bersanelli, P. Bielewicz, C. A. Bischoff, J. J. Bock, A. Bonaldi, L. Bonavera, J. R. Bond, J. Borrill, F. R. Bouchet, F. Boulanger, J. A. Brevik, M. Bucher, I. Buder, E. Bullock, C. Burigana, R. C. Butler, V. Buza, E. Calabrese, J.-F. Cardoso, A. Catalano, A. Challinor, R.-R. Chary, H. C. Chiang, P. R. Christensen, L. P. L. Colombo, C. Combet, J. Connors, F. Couchot, A. Coulais, B. P. Crill, A. Curto, F. Cuttaia, L. Danese, R. D. Davies, R. J. Davis, P. de Bernardis, A. de Rosa, G. de Zotti, J. Delabrouille, J.-M. Delouis, F.-X. Désert, C. Dickinson, J. M. Diego, H. Dole, S. Donzelli, O. Doré, M. Douspis, C. D. Dowell, L. Duband, A. Ducout, J. Dunkley, X. Dupac, C. Dvorkin, G. Efstathiou, F. Elsner, T. A. Enßlin, H. K. Eriksen, E. Falgarone, J. P. Filippini, F. Finelli, S. Fliescher, O. Forni, M. Frailis, A. A. Fraisse, E. Franceschi, A. Frejsel, S. Galeotta, S. Galli, K. Ganga, T. Ghosh, M. Giard, E. Gjerløw, S. R. Golwala, J. González-Nuevo, K. M. Górski, S. Gratton, A. Gregorio, A. Gruppuso, J. E. Gudmundsson, M. Halpern, F. K. Hansen, D. Hanson, D. L. Harrison, M. Hasselfield, G. Helou, S. Henrot-Versillé, D. Herranz, S. R. Hildebrandt, G. C. Hilton, E. Hivon, M. Hobson, W. A. Holmes, W. Hovest, V. V. Hristov, K. M. Huffenberger, H. Hui, G. Hurier, K. D. Irwin, A. H. Jaffe, T. R. Jaffe, J. Jewell, W. C. Jones, M. Juvela, A. Karakci, K. S. Karkare, J. P. Kaufman, B. G. Keating, S. Kefeli, E. Keihänen, S. A. Kernasovskiy, R. Keskitalo, T. S. Kisner, R. Kneissl, J. Knoche, L. Knox, J. M. Kovac, N. Krachmalnicoff, M. Kunz, C. L. Kuo, H. Kurki-Suonio, G. Lagache, A. Lähteenmäki, J.-M. Lamarre, A. Lasenby, M. Lattanzi, C. R. Lawrence, E. M. Leitch, R. Leonardi, F. Levrier, A. Lewis, M. Liguori, P. B. Lilje, M. Linden-Vørnle, M. López-Caniego, P. M. Lubin,

- M. Lueker, J. F. Macías-Pérez, B. Maffei, D. Maino, N. Mandolcsi, A. Mangilli, M. Maris, P. G. Martin, E. Martínez-González, S. Masi, P. Mason, S. Matarrese, K. G. Megerian, P. R. Meinhold, A. Melchiorri, L. Mendes, A. Mennella, M. Migliaccio, S. Mitra, M.-A. Miville-Deschénes, A. Moneti, L. Montier, G. Morgante, D. Mortlock, A. Moss, D. Munshi, J. A. Murphy, P. Naselsky, F. Nati, P. Natoli, C. B. Netterfield, H. T. Nguyen, H. U. Nørgaard-Nielsen, F. Noviello, D. Novikov, I. Novikov, R. O'Brient, R. W. Ogburn, A. Orlando, L. Pagano, F. Pajot, R. Paladini, D. Paoletti, B. Partridge, F. Pasian, G. Patanchon, T. J. Pearson, O. Perdereau, L. Perotto, V. Pettorino, F. Piacentini, M. Piat, D. Pietrobon, S. Plaszczynski, E. Pointecouteau, G. Polenta, N. Ponthieu, G. W. Pratt, S. Prunet, C. Pryke, J.-L. Puget, J. P. Rachen, W. T. Reach, R. Rebolo, M. Reinecke, M. Remazeilles, C. Renault, A. Renzi, S. Richter, I. Ristorcelli, G. Rocha, M. Rossetti, G. Roudier, M. Rowan-Robinson, J. A. Rubiño Martín, B. Rusholme, M. Sandri, D. Santos, M. Savelainen, G. Savini, R. Schwarz, D. Scott, M. D. Seiffert, C. D. Sheehy, L. D. Spencer, Z. K. Staniszewski, V. Stolyarov, R. Sudiwala, R. Sunyaev, D. Sutton, A.-S. Suur-Uski, J.-F. Sygnet, J. A. Tauber, G. P. Teply, L. Terenzi, K. L. Thompson, L. Toffolatti, J. E. Tolan, M. Tomasi, M. Tristram, M. Tucci, A. D. Turner, L. Valenziano, J. Valiviita, B. Van Tent, L. Vibert, P. Vielva, A. G. Vieregg, F. Villa, L. A. Wade, B. D. Wandelt, R. Watson, A. C. Weber, I. K. Wehus, M. White, S. D. M. White, J. Willmert, C. L. Wong, K. W. Yoon, D. Yvon, A. Zacchei, and A. Zonca. Joint analysis of bicep2/ *Keck Array* and *Planck* data. *Phys. Rev. Lett.*, 114:101301, Mar 2015.
- [2] K. J. Åström and R. M. Murray. *Feedback Systems: An Introduction for Scientists and Engineers*. Princeton University Press, 2008.
- [3] G. Batey and G. Teleberg. Principles of dilution refrigeration. Technical report, Oxford Instruments NanoScience, Tubney Woods, Abingdon, Oxon, OX13 5QX, United Kingdom, 2015.
- [4] J. Bock, S. Church, M. Devlin, G. Hinshaw, A. Lange, A. Lee, L. Page, B. Partridge, J. Ruhl, M. Tegmark, P. Timbie, R. Weiss, B. Winstein, and M. Zaldarriaga. Task Force on Cosmic Microwave Background Research. *ArXiv Astrophysics e-prints*, 2006.

- [5] J.-A. Brown. P457: Wave polarisation and stokes parameters. online, 2008. Accessed from [http://www.ras.ucalgary.ca/~jocat/polarisation\\_2008.pdf](http://www.ras.ucalgary.ca/~jocat/polarisation_2008.pdf) on 4/8/2016.
- [6] P. Cabella and M. Kamionkowski. Theory of cosmic microwave background polarization. In *International School of Gravitation and Cosmology: The Polarization of the Cosmic Microwave Background Rome, Italy, September 6-11, 2003*, 2004.
- [7] D. T. Chuss, E. J. Wollack, R. Henry, H. Hui, A. J. Juarez, M. Krejny, S. H. Moseley, and G. Novak. Properties of a variable-delay polarization modulator. *Appl. Opt.*, 51(2):197–208, Jan 2012.
- [8] S. Clesse. An introduction to inflation after Planck: from theory to observations. In *Proceedings, 10th Modave Summer School on Mathematical Physics*, 2015.
- [9] J. R. Eimer. *The Cosmology Large Angular Scale Surveyor (CLASS): In Search of the Energy Scale of Inflation*. PhD thesis, Johns Hopkins University, January 2013.
- [10] T. Essinger-Hileman, A. Ali, M. Amiri, J. W. Appel, D. Araujo, C. L. Bennett, F. Boone, M. Chan, H.-M. Cho, D. T. Chuss, F. Colazo, E. Crowe, K. Denis, R. Dnner, J. Eimer, D. Gothe, M. Halpern, K. Harrington, G. C. Hilton, G. F. Hinshaw, C. Huang, K. Irwin, G. Jones, J. Karakla, A. J. Kogut, D. Larson, M. Limon, L. Lowry, T. Marriage, N. Mehrle, A. D. Miller, N. Miller, S. H. Moseley, G. Novak, C. Reintsema, K. Rostem, T. Stevenson, D. Towner, K. U-Yen, E. Wagner, D. Watts, E. J. Wollack, Z. Xu, and L. Zeng. Class: the cosmology large angular scale surveyor. *Proc. SPIE*, 9153:91531I–91531I–23, 2014.
- [11] D. Griffiths. *Introduction to Electrodynamics*. Pearson Education Inc., 4 edition, 2013.
- [12] A. H. Guth. Inflationary universe: A possible solution to the horizon and flatness problems. *Physical Review D*, 23, 1981.
- [13] M. Hansen. Achieving accurate on-wafer flicker noise measurements through 30 mhz. Technical report, Cascade Microtech, INC, 9100 SW Gemini Dr, Beaverton OR, 97008, USA, 5 2009.
- [14] E. Hecht. *Optics*. Pearson Education Inc., 4 edition, 2002.

- [15] G. Hinshaw, D. Larson, E. Komatsu, D. N. Spergel, C. L. Bennett, J. Dunkley, M. R. Nolta, M. Halpern, R. S. Hill, N. Odegard, L. Page, K. M. Smith, J. L. Weiland, B. Gold, N. Jarosik, A. Kogut, M. Limon, S. S. Meyer, G. S. Tucker, E. Wollack, and E. L. Wright. Nine-year wilkinson microwave anisotropy probe (wmap) observations: Cosmological parameter results. *The Astrophysical Journal Supplement Series*, 208(2):19, 2013.
- [16] W. Hu and S. Dodelson. Cosmic microwave background anisotropies. *Annual Review of Astronomy and Astrophysics*, 40, 2002.
- [17] W. Hu and M. White. A CMB polarization primer. *New Astronomy*, 2, 1997.
- [18] K. Ichiki. Cmb foreground: A concise review. *Progress of Theoretical and Experimental Physics*, 2014(6), 2014.
- [19] Inductiveload. Polarisation ellipse2, 2008. Accessed May 2016, Public Domain Image.
- [20] R. Keisler et al. Measurements of Sub-degree B-mode Polarization in the Cosmic Microwave Background from 100 Square Degrees of SPTpol Data. *Astrophys. J.*, 807(2):151, 2015.
- [21] A. Kosowsky. Introduction to microwave background polarization. *New Astronomy*, 43, 1999.
- [22] A. Kusaka, T. Essinger-Hileman, J. W. Appel, P. Gallardo, K. D. Irwin, N. Jarosik, M. R. Nolta, L. A. Page, L. P. Parker, S. Raghunathan, J. L. Sievers, S. M. Simon, S. T. Staggs, and K. Visnjic. Modulation of cosmic microwave background polarization with a warm rapidly rotating half-wave plate on the atacama b-mode search instrument. *Review of Scientific Instruments*, 85(2), 2014.
- [23] N. Lobontiu. *Compliant Mechanisms: Design of Flexure Hinges*. CRC Press, 1 edition, 2002.
- [24] L. Lowry. Testing and optimization analysis of the class variable-delay polarization modulators. Undergraduate Senior Thesis, 5 2013.
- [25] T. Marriage. Vpm stroke analysis. Technical report, Johns Hopkins University, July 2013.
- [26] Mets501. Helium phase diagram. Accessed May 2016, used under CC BY-SA 3.0.

- 
- [27] N. J. Miller, D. T. Chuss, T. A. Marriage, E. J. Wollack, J. W. Appel, C. L. Bennett, J. Eimer, T. Essinger-Hileman, D. J. Fixsen, K. Harrington, S. H. Moseley, K. Rostem, E. R. Switzer, and D. J. Watts. Recovery of large angular scale cmb polarization for instruments employing variable-delay polarization modulators. *The Astrophysical Journal*, 818(2):151, 2016.
  - [28] D. Moulton. Stokesparameters, 2008. Accessed May 2016, Used under CC BY-SA 3.0.
  - [29] NASA. End of univerese. Accessed May 2016, Public Domain Image.
  - [30] NASA/WMAP Science Team. Nine Year Microwave Sky. Accessed May 2016.
  - [31] R. Richardson and B. Evans. A review of pulse tube refrigeration. *International Journal of Refrigeration*, 20(5):367 – 373, 1997.
  - [32] B. Ryden. *Introduction to Cosmology*. Pearson Education Inc., 2003.
  - [33] E. Siegel. What are the odds? Part 2: Cosmic Inflation. accessed May 2016.
  - [34] TheAstronomyBum. The History of the Universe, 2014. Accessed May 2016, Used under CC0 1.0.
  - [35] D. J. Watts et al. Measuring the Largest Angular Scale CMB B-mode Polarization with Galactic Foregrounds on a Cut Sky. *Astrophys. J.*, 814(2):103, 2015.